Soil Dynamics and Earthquake Engineering 142 (2021) 106566

Contents lists available at ScienceDirect

Soil Dynamics and Earthquake Engineering

journal homepage: http://www.elsevier.com/locate/soildyn

Effect of vertical input motion and excess pore pressures on the seismic performance of a zoned dam

Ernesto Cascone [a], Giovanni Biondi [a,*], Domenico Aliberti [a], Sebastiano Rampello [b]

[a] Department of Engineering, University of Messina, Contrada di Dio, S. Agata, 98166, Messina, Italy
[b] Department of Structural and Geotechnical Engineering (DISG), Sapienza University of Rome, Via Eudossiana 18, 00184, Rome, Italy

ARTICLE INFO

Keywords:
Dynamic analysis
Earth dam
Seismic performance
Pore pressure build-up
Vertical input motion

ABSTRACT

This paper investigates the combined effect of the vertical component of the input motion and of the weakening effect associated to pore-pressure build-up with reference to a zoned earth dam for which the most recent probabilistic seismic hazard analyses promoted the need of evaluating its seismic performance.

The two effects were studied through advanced plane-strain non-linear dynamic analyses using a finite-difference numerical model calibrated on an accurate geotechnical characterisation. The occurrence of ultimate limit states in the dam embankment is checked using sets of horizontal and vertical input motions properly selected to account for possible frequency coupling with the dam.

The analysis results are presented and discussed in the paper focusing on (i) the main features of the plastic mechanisms temporarily induced by the seismic actions, (ii) the amplification of the horizontal and vertical accelerations acting in the dam body, (iii) the role of the energy and frequency content of the input motion on the magnitude of earthquake-induced permanent displacements, (iv) the combined effect of frequency coupling and non-linear soil behaviour on the overall dam response.

1. Introduction

The combined effects of the vertical input motion and earthquake-induced pore pressure build-up on the seismic performance of earth dams, are rarely dealt with in the scientific literature. In this vein, a set of non-linear finite difference dynamic analyses of an earth dam have been carried out considering, separately or contemporarily, the effects of the vertical input motion and the occurrence of seismic-induced excess pore pressures.

The analyses focus on the acceleration amplification and deformation patterns in the dam body and on the magnitude of earthquake-induced permanent displacements. The results are discussed in the light of the combined effect of frequency coupling, energy content of the input motion and non-linear soil behaviour and, even if related to a specific dam, namely the San Pietro dam, are presented in a general framework trying to provide outcomes of general validity and of broad interest for dam engineers.

The San Pietro dam is a large zoned earth dam built between 1958 and 1964 in Campania (Italy), an area of high seismicity according to the most recent probabilistic seismic hazard assessment (*PSHA*) transposed into the latest Italian codes relevant for seismic analyses of new and existing dams [1,2]. The dam was designed before the establishment of a seismic code and, since it is still in use, the assessment of its seismic safety and post-seismic serviceability is of great interest.

The main cross section of the dam is shown in Fig. 1a. The geotechnical characterisation together with a set of static and seismic simplified preliminary analyses, as well as the selected input motions and the performance indexes adopted to check the seismic performance of the dam are described by Biondi et al. [3].

Consistently with ICOLD [4] guidelines and according to the *Italian Building Code* (NTC18) [1] and the *Italian Code for Dams* (NTD14) [2], the seismic response of the dam was examined using procedures characterised by an increasing level of complexity, which included pseudo-static analyses, coupled and de-coupled Newmark-type displacement analyses and finite-difference non-linear dynamic response analyses.

This paper describes the results of the plane strain dynamic analyses performed for the seismic scenarios prescribed by the Italian codes [1,2] for the *Life Safety Limit State* (*LLS*) and the *Collapse Limit State* (*CLS*). The limit conditions to be achieved for attaining these limit states fit well the performance criteria introduced by ICOLD [5] with reference to the *Safety Evaluation Earthquake* (*SEE*) and the *Operating Basis Earthquake*

* Corresponding author.
E-mail address: gbiondi@unime.it (G. Biondi).

https://doi.org/10.1016/j.soildyn.2020.106566
Received 9 May 2020; Received in revised form 27 September 2020; Accepted 25 December 2020
Available online 10 January 2021

(*OBE*).

Since seismic stability of dams located in near- and far-fault areas is an issue of paramount concern, results of several advanced dynamic analyses are available in the literature with reference to earth (e.g. Ref. [6]), rockfill (e.g. Ref. [7]) and concrete (e.g. Ref. [8]) dams.

Advanced dynamic non-linear analyses have been also carried out for the San Pietro dam [e.g. 9–10] using input motions selected through a proper mix of seismic historical data and results of a seismic hazard study updated to the end of the last century. The results of these studies and those of the screening-level seismic analyses [3], together with the severe seismic actions recently estimated by the probabilistic seismic hazard analysis available for the dam site, motivate the dynamic analyses discussed in this paper to examine the combined effect of the pore water pressure build-up in the materials of the dam and of the vertical component of the input motion. The constitutive assumptions adopted in the analyses were selected to provide an insight into these aspects while keeping the complexity of the analyses at a level comparable to that characterising modern best practice in dam engineering. This pragmatic

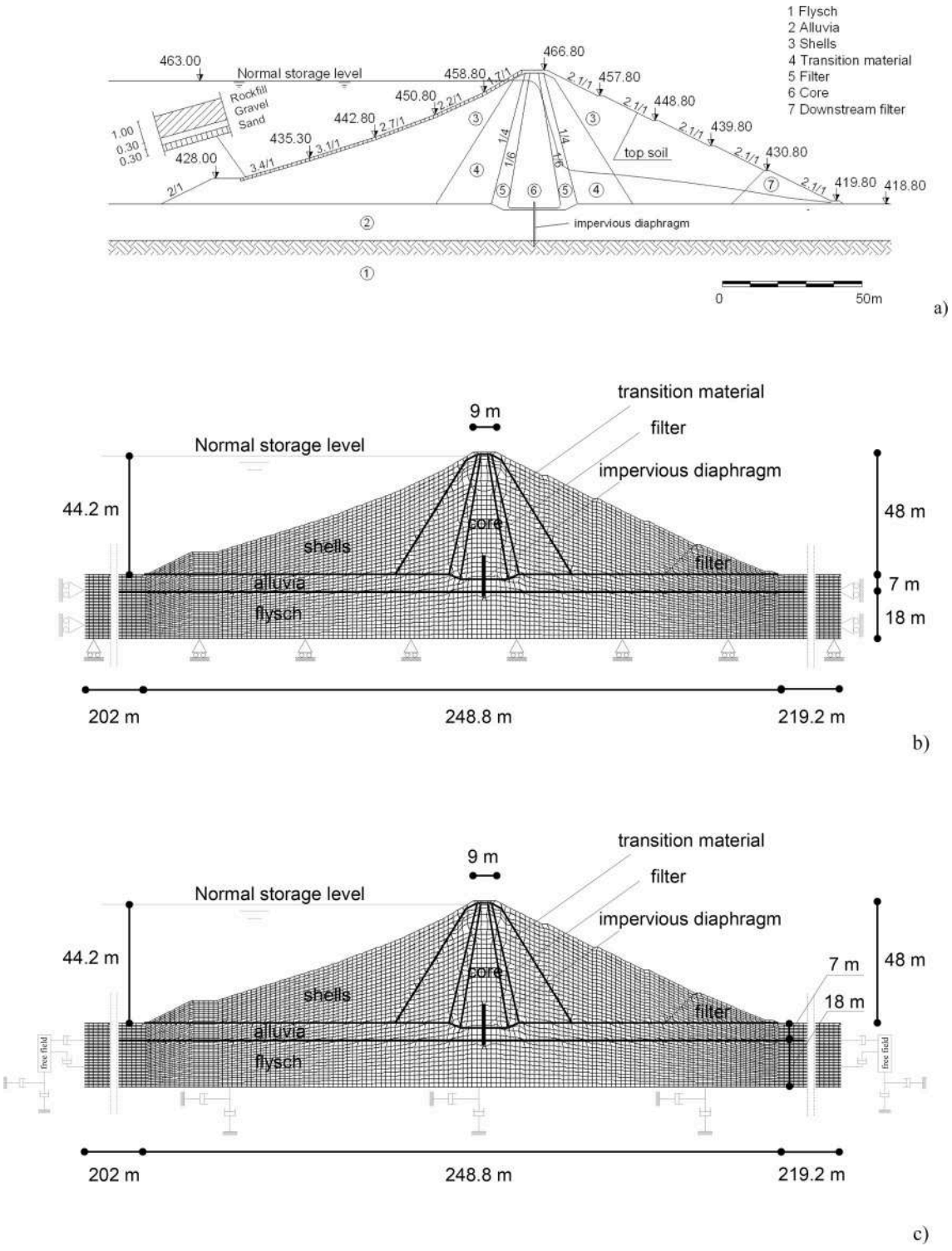

Fig. 1. a) Main cross section of the dam; b,c) finite difference grid and boundary conditions adopted in the static (b) and dynamic (c) analyses.

choice was driven by the intention of providing research outcomes relevant to design issues that could be directly adopted in engineering practice.

2. Numerical modelling

The plane-strain dynamic analyses of the seismic response of the dam were carried out in the time domain and in terms of effective stresses using the code FLAC 2D v.7.0 [11].

A set of preliminary static analyses, aimed at reproducing the total and the effective state of stress at the end of the stages of dam construction [3], including a steady-state seepage analysis which provided the water table shown in Fig. 1a, preceded the dynamic analyses carried out modelling the reservoir as a hydrostatic load applied on the upstream face of the dam.

The dynamic analyses were performed accounting for the non-linear soil behaviour, assuming values of the small-strain shear modulus G_0 evaluated from the cross-hole tests and considering a hysteretic soil model (§ 2.2), additional Rayleigh damping (§ 2.3), excess pore-pressure generation (§ 2.4) and input motions consistent with the seismicity of the dam site (§ 2.5), as discussed in the following together with the boundary conditions adopted in the analyses (§ 2.1).

2.1. Numerical model

The numerical analyses were carried out discretising the dam and the foundation soils via a finite difference grid of 13,845 quadrilateral elements. The grid extends about three times the width of the embankment base, to ensure a negligible interaction of the dam with the vertical boundaries and to a depth of 25 m from the embankment base, including 18 m of the stiff formation assumed as the seismic bedrock in the dynamic analyses.

Fig. 1 b,c shows the grid and the boundary conditions adopted in the static (Fig. 1b) and dynamic (Fig. 1c) analyses.

In the static analyses (Fig. 1b), displacements in both directions were restrained at the bottom boundary of the finite difference grid and horizontal displacements were restrained at its lateral sides. The adopted fixed constraints provide the reaction forces which ensure the static equilibrium and are placed at a distance from the region of interest for the dam which allows to minimize their influence on the numerical results.

Under dynamic loading conditions, such boundaries cause reflection of outward propagating waves back into the numerical model, not allowing the energy radiation. Also, the boundary condition at the side of the model must account for the free-field motion that would exist in the absence of the dam and of the reservoir.

To address both these aspects the use of supplementary free-field grids, coupled to the lateral boundaries of the main grid of the model (Fig. 1c), was combined with the technique of absorbing boundaries applied using the well-known Lysmer & Kuhlemeyer viscous boundaries. Specifically, according to the procedure originally proposed by Cundall et al. [12] and implemented in FLAC, at the lateral sides of the main grid the required free-field conditions have been enforced in such a way that boundaries retain their non-reflecting properties and outward waves originating from the dam are properly absorbed.

The free-field model consists of supplementary straight and vertical soil columns of unit width (free-field grids), simulating the behaviour of the extended medium, having the same height of the lateral boundaries of the main-grid and discretised into the same number of elements which are in a state of uniform strain and stress.

The lateral boundaries of the main-grid are coupled to the two free-field grids by viscous dashpots, which absorb energy in a manner similar to the action of quiet boundaries, and the unbalanced forces from the free-field grids are applied to the main grid boundary replacing the actions provided by the elementary-constraints used in the static analysis.

In this way, plane waves propagating upward suffer no distortion at the boundary because the free-field grid supplies conditions that are identical to those of an infinite model.

Finally, Lysmer & Kuhlemeyer viscous boundaries, consisting in independent dashpots in the normal and shear direction at the model boundaries, were introduced at the bottom of the main grid, replacing the elementary-constraints used in the static analysis, and at the bottom of the free-field grids.

The maximum height of the main-grid elements (and thus also of the supplementary free-field grids) was set smaller than 1/6 of the wavelength associated to the highest frequency of the input motions used in the dynamic analyses to avoid numerical distortion of the propagating waves.

2.2. Hysteretic model

The non-linear and dissipative soil behaviour was described using the hysteretic model *Sigmoidal 3* available in the FLAC library. Previous studies (e.g. Ref. [13]) showed that this model coupled with the Mohr-Coulomb failure criterion permits to successfully capture the seismic behaviour of earth dams in terms of deformation mechanisms, permanent displacements and acceleration amplification.

In the *Sigmoidal 3* model the normalised shear modulus G/G_0 is expressed as a function of the shear strain γ by the relationship:

$$\frac{G}{G_0} = \frac{1}{1 + e^{\left(\frac{c+\log\gamma}{b}\right)}} \tag{1}$$

where coefficients b and c are model parameters.

To calibrate the model for the fine-grained soils of the core, the two resonant column (*RC*) tests carried out at confining pressures of 150 and 300 kPa (Fig. 2) were used; excess pore pressure measurements are not available for the test performed at $p' = 150$ kPa.

Unfortunately, neither resonant column tests nor other cyclic tests were performed on materials of the shells and of the foundation soils during the geotechnical characterisation, so in the analyses it was necessary to use data selected from the literature.

As far as the shells are concerned, the grain size of the coarse materials they are made of fairly resembles the grain size distribution of the materials investigated by Rollins et al. [14] using confining pressures in the range 30–490 kPa, which adequately represents the range of stress levels in the shell materials. Thus, the lower bound of the experimental $G/G_0 - \gamma$ curves by Rollins et al. [14] was used for the shells, since this choice provides a conservative estimate of both deformations and displacements suffered by the dam.

In the 7 m thick layer of alluvial soil underneath the dam the small strain shear modulus G_0 varies in the range 650–1050 MPa, with higher values under the dam centre line, whereas in the bedrock formation G_0 is larger than 1300 MPa. Thus, for the stiff foundation soils the experimental data by Seed & Idriss [15] relative to rocklike materials were considered suitable to describe their behaviour.

In Fig. 2 the curves proposed by Vucetic & Dobry [16] for values of plasticity index $PI = 15$, 30 and 50% are compared with the *RC* test results showing the best agreement with the curve at $PI = 50\%$, despite the soil samples retrieved from the core of the dam are characterised by an average value of $PI = 21.5\%$. This occurrence may be possibly attributed to the circumstance that the curves proposed by Vucetic & Dobry [16] were obtained on natural soils, whereas the materials of the core are artificially compacted clayey soils.

The calibration of the parameters (b, c) ruling the hysteretic model *Sigmoidal 3* (Eq. (1)) was accomplished by fitting the experimental curves that describe the variation of the normalised shear modulus G/G_0 with the shear strain γ. Damping was instead obtained from hysteresis loops modelled using Masing criteria, also implemented in the model.

For the soils of the shells, the core and the dam foundation, Table 1 provides the model parameters b and c obtained from the calibration

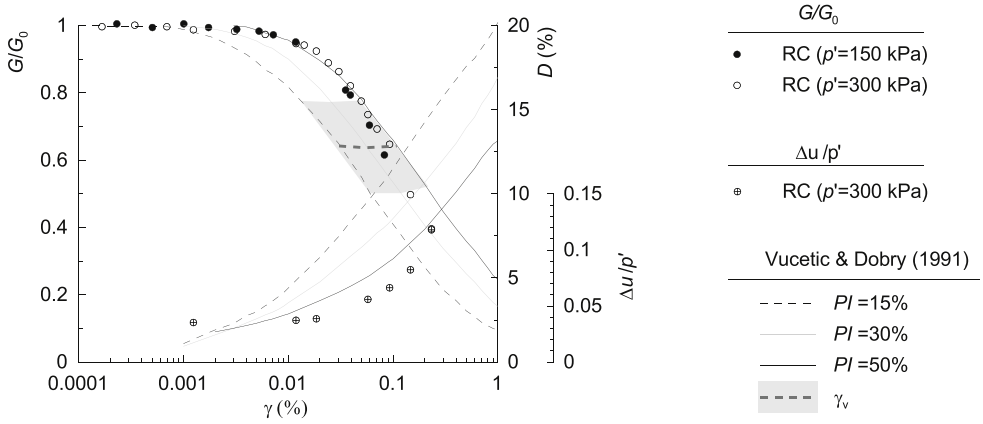

Fig. 2. Resonant Column test results and data from literature.

Table 1
Parameters of Eq. (1).

material	experimental data	*b*	*c*
Shells	Rollins et al. [14] - lower limit	0.506	1.718
Core	*RC* test results [3]	0.454	0.714
Foundation	Seed & Idriss [15]	0.748	0.156

procedure while Fig. 3 shows the comparison between the selected sets of experimental data in terms of stiffness and damping (represented by symbols) and the $G/G_0 - \gamma$ and $D - \gamma$ curves provided by the hysteretic model (solid lines).

It is apparent that, in the range of medium to large shear strains, this stiffness-calibrated hysteretic models lead to damping curves different from those corresponding to the selected set of experimental data: a relevant overprediction of damping can be observed for the soils of the shells (Fig. 3 a) and the core (Fig. 3 b), while damping is slightly underpredicted for the foundation soils (Fig. 3 c).

To assess the influence of these discrepancies on the computed dam response, two additional calibration procedures of the *Sigmoidal 3* model were examined and preliminary dynamic analyses of the dam were performed, as discussed in the Appendix, showing that the model parameters calibrated on the $G/G_0 - \gamma$ curves provided the most conservative assessment of the dam response.

2.3. Rayleigh damping

The hysteretic damping provided by the adopted constitutive model is very small in the range of low shear strains, in that $D - \gamma$ curves characterised by $D \approx 0$ for $\gamma < 0.001\%$ are computed, these being not capable to reproduce the actual damping D_0 at very small shear strains.

Accordingly, for all the materials involved in the analyses, an additional viscous damping was introduced using the frequency-dependent Rayleigh formulation in which the damping matrix has two components linearly proportional to the mass and stiffness matrices through a mass-proportional a and a stiffness-proportional b damping constants. As usual, a and b were selected to minimize the variation with frequency of the modal damping ratio ξ_i associated to the i^{th} mode of vibration of the dam obtaining an approximately frequency-independent additional damping over a given range of frequencies. This leads to $a = \xi_{min} \cdot \omega_{min}$ and $b = \xi_{min}/\omega_{min}$, ξ_{min} being the minimum value of ξ_i occurring at a circular frequency $\omega_{min} = 2 \cdot \pi \cdot f_{min}$. The frequency f_{min} was set equal to the first natural frequency of horizontal elastic vibration of the dam f_{1e}, evaluated from the largest peak of the undamped elastic transfer function of the dam. This latter was computed, using a white noise input motion, as the ratio between the amplitude Fourier spectra of acceleration computed at the crest and the base of the dam, along its axis: $f_{1e} =$ 3.12 Hz was evaluated that is in a fair agreement with the values obtained using the solutions proposed by Dakoulas & Gazetas [17] ($f_{1e} =$ 3.39 Hz) and Papadimitriu et al. [18] ($f_{1e} =$ 3.30 Hz). A damping coefficient $\xi_{min} = 1.7\%$ was assumed that permits to simulate the damping at small shear strains ($\gamma < 0.001\%$) for all the materials of the dam (Fig. 3). Accordingly, it is $a = 33.33$ and $b = 0.087$.

2.4. Excess pore pressure generation model

Possible occurrence of excess pore pressure induced by earthquake loading was ignored in the alluvial soils underneath the dam, improved by concrete injections prior to dam construction. Conversely, for the soils of the shells and the core, pore water pressure build-up was accounted for in the analyses through the so-called *Finn model* [19]. The model describes the incremental shear-volume coupling through an equation developed for sands under simple shear loading conditions and it is available in the library of the code FLAC in the formulation proposed by Byrne [20] for fully saturated soils. In the model, the excess pore pressure Δu generated in an increment of undrained loading is related, through the constrained bulk modulus M_r, to the corresponding increment in volumetric strain $\Delta\varepsilon_{vd}$ that would have occurred in the same loading increment under drained conditions:

$$\Delta u = M_r \cdot \Delta\varepsilon_{vd} \tag{2}$$

The bulk modulus M_r and the volumetric strain increment $\Delta\varepsilon_{vd}$ were evaluated through the following equations:

$$\frac{M_r}{p_a} = K_m \cdot \left(\frac{\sigma'_v}{p_a}\right)^m \tag{3}$$

$$\Delta\varepsilon_{vd} = \gamma \cdot C_1 \cdot \exp\left[-C_2\left(\frac{\varepsilon_{vd}}{\gamma}\right)\right] \tag{4}$$

where σ'_v and σ'_{v0} are the current and the initial vertical effective stresses, γ and ε_{vd} are the cyclic shear and volumetric strains, respectively, $m = 0.5$ and $K_m = 1600$ are material constants and p_a is the atmospheric pressure.

According to Byrne [20] the constant C_1, that controls the amount of volume change, can be related to the soil relative density D_R in the form:

$$C_1 = 7600 \cdot (D_R)^{-2.5} \tag{5}$$

And, regardless the soil relative density, $C_2 = 0.4/C_1$ can be assumed.

Despite the selected model of pore water pressure build up was originally referred to the cyclic behaviour of loose sands, several studies showed that its numerical formulation can be suitably adopted to predict the excess pore pressure induced by cyclic loading in medium to dense sandy soils (e.g. Ref. [21]) and in sandy gravels (e.g. Ref. [22]).

According to the standard penetration tests (*SPT*) carried out in the

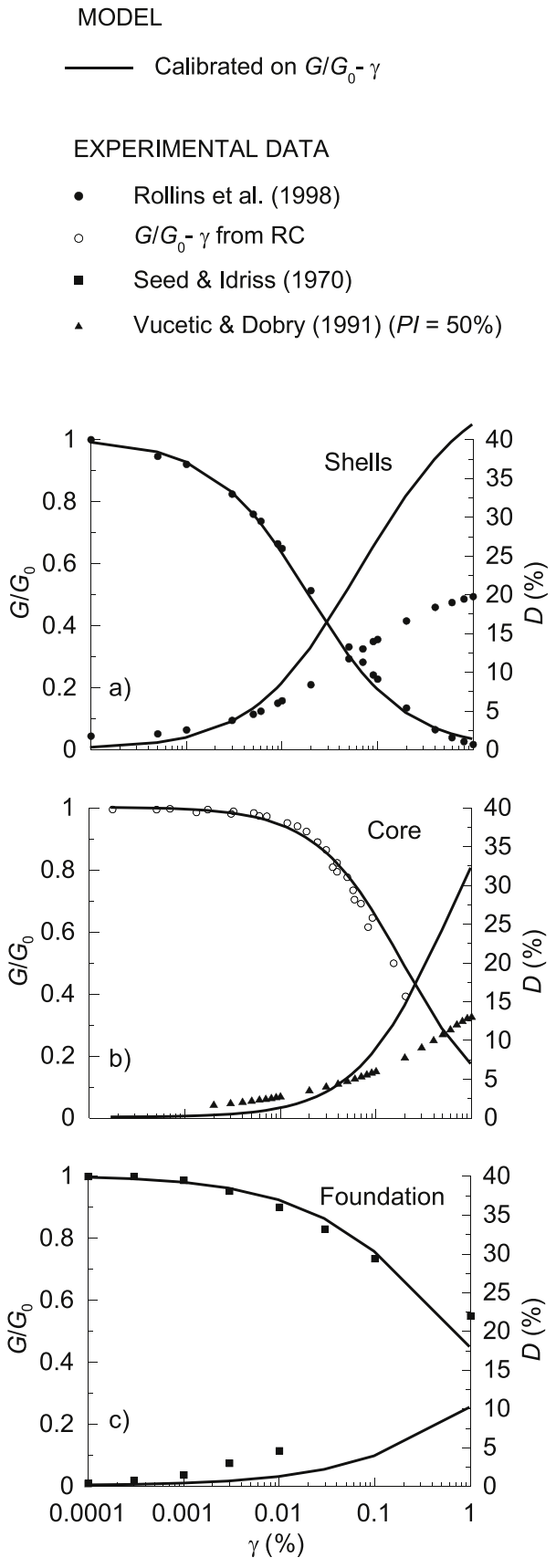

Fig. 3. Calibration of *Sigmoidal 3* model for the shells (a), the core (b) and the foundation soil (c) based on the normalised stiffness data.

foundation soils and shells of the dam an average relative density D_R = 95% was assumed for the alluvial gravels, providing $C_1 = 0.086$ and $C_2 = 4.651$, and $D_R = 60\%$ was assumed for the shells, leading to $C_1 = 0.273$ and $C_2 = 1.465$.

The same model of pore water pressure build-up (Eqs. (2)–(4)) was adopted for the fine-grained soils of the core, mainly consisting of sandy silts. For these soils, the *RC* tests were simulated through the computer code FLAC, using the hysteretic model previously described (§ 2.1), and the parameters $C_1 = 0.185$ and $C_2 = 2.158$ were evaluated matching the experimental $\Delta u/p' - \gamma$ relationship shown in Fig. 2.

2.5. Input motions

The input motions adopted in the dynamic analyses consist of filtered horizontal and vertical components of acceleration time-histories recorded on stiff horizontal rock outcropping (soil class *A*) and were selected from worldwide databases of earthquake records (Table 2).

A comprehensive description of these motions and of the selection and scaling criteria is provided in Ref. [3]: the main information is summarised in the following.

Two sets of acceleration records were selected with reference to the *Life Safety Limit State* (*LLS*) and the *Collapse Limit State* (*CLS*) mandatorily prescribed by relevant Italian codes [1,2] as limit states to be checked for existing dams.

The reference seismic actions for these limit states are characterised by mean return periods T_R = 949 and 1950 years, for the *LLS* and the *CLS*, respectively, with corresponding values of the expected peak horizontal acceleration at the dam site $a_{g,T} = 0.304g$ (*LLS*) and $0.414g$ (*CLS*).

The horizontal components of the selected records were scaled up to the above-mentioned reference values; the vertical ones were scaled using the same scale factor adopted for the corresponding horizontal component. Thus, two sets of accelerograms were obtained for the *CLS* (records #1 … #5) and the *LLS* (records #3 … #7); some of the records (#3, #4, #5) match the selection criteria for both the *LLS* and the *CLS* even if they were scaled up to different peak values for each different limit state. Each time-history was filtered with a 10 Hz low-pass Butterworth filter to reduce the high frequency content, not reproducible in the numerical analysis and not affecting the predictions of dam response.

The time histories of the horizontal (a_h) and vertical (a_v) components of the scaled acceleration records and the corresponding smoothed Fourier amplitude spectra are plotted in Figs. 4 and 5 respectively. The first natural frequency of horizontal (f_{1e} = 3.12 Hz) and vertical ($f^v_{1e} = 4.54$ Hz) elastic vibration of the dam are also indicated in Fig. 5.

The spectra of Fig. 5 a-g show that records #1, #2, #4 and #7 are characterised by one ($f_p \approx 1.8 \div 2.8$ Hz) or two dominant frequencies while the remaining records exhibit a broad band frequency content.

Concerning the vertical components (Fig. 5 h-p), a frequency f_p = 2.1–2.9 Hz substantially lower than f^v_{1e} predominates for the vertical records #1 and #2, while a broad band frequency content generally characterises the spectra of the remaining time histories of vertical acceleration.

Table 2
Earthquake records selected for the analyses.

#	Earthquake	Station, record, earthquake data	M_w	R_{jb} (km)
1	Loma Prieta	Gilroy Array # 1, 000, October 18, 1989	6.9	8.84
2	Loma Prieta	Gilroy Array # 1, 090, October 18, 1989	6.9	8.84
3	Parkfield −02 CA	Parkfield – Turkey Flat # 1, 270, September 28, 2004	6.0	4.66
4	Parkfield −02 CA	Parkfield – Turkey Flat # 1, 360, September 28, 2004	6.0	4.66
5	Northridge	Wonderland Ave, 185, January 17, 1994	6.7	15.11
6	Iwate, Japan	IWT010, NS, June 13, 2008	6.9	16.26
7	Tottori, Japan	SMNH10, EW, October 06, 2000	6.6	15.58

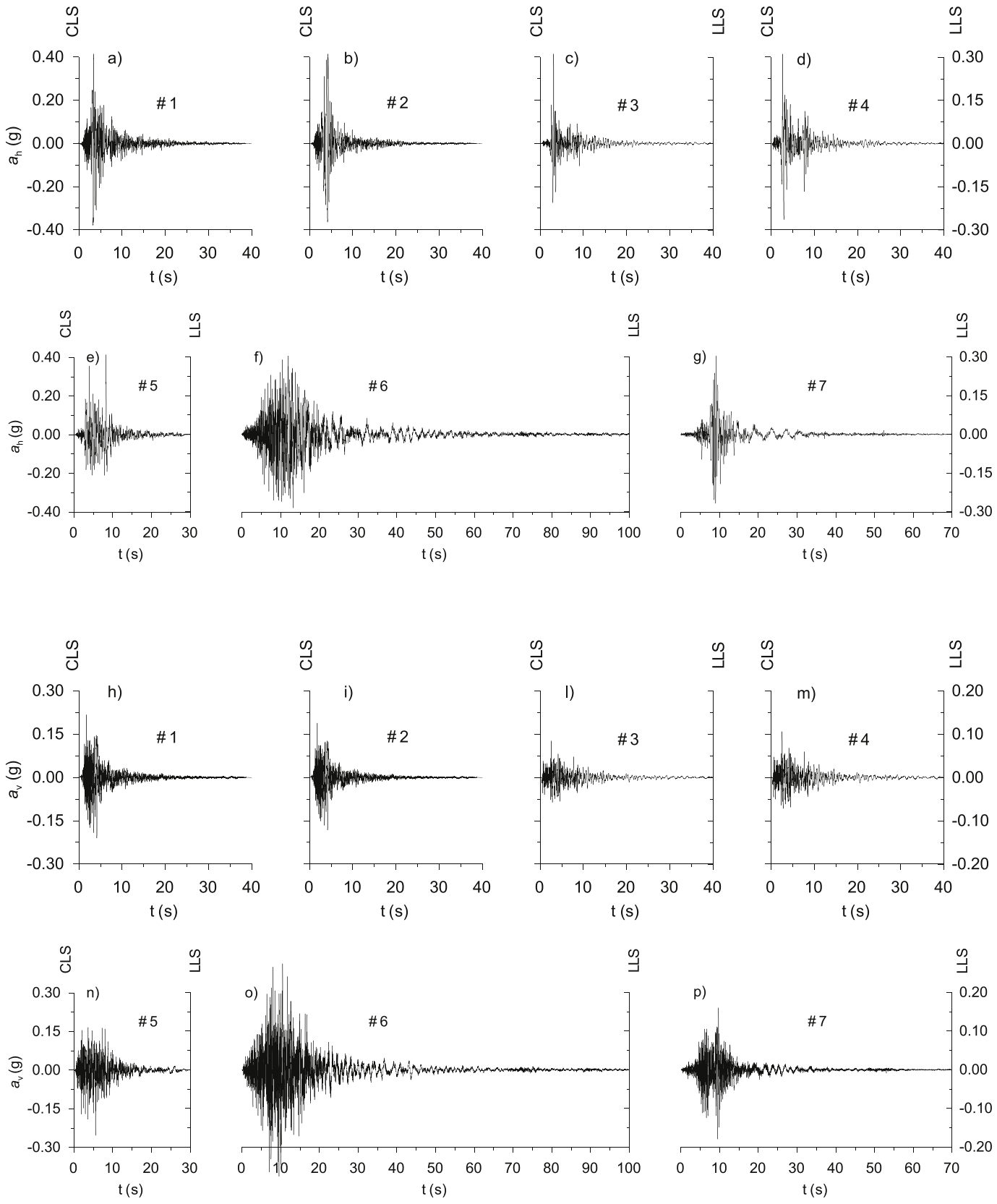

Fig. 4. Acceleration time histories of the horizontal (a–g) and vertical (h–p) components of the scaled seismic records.

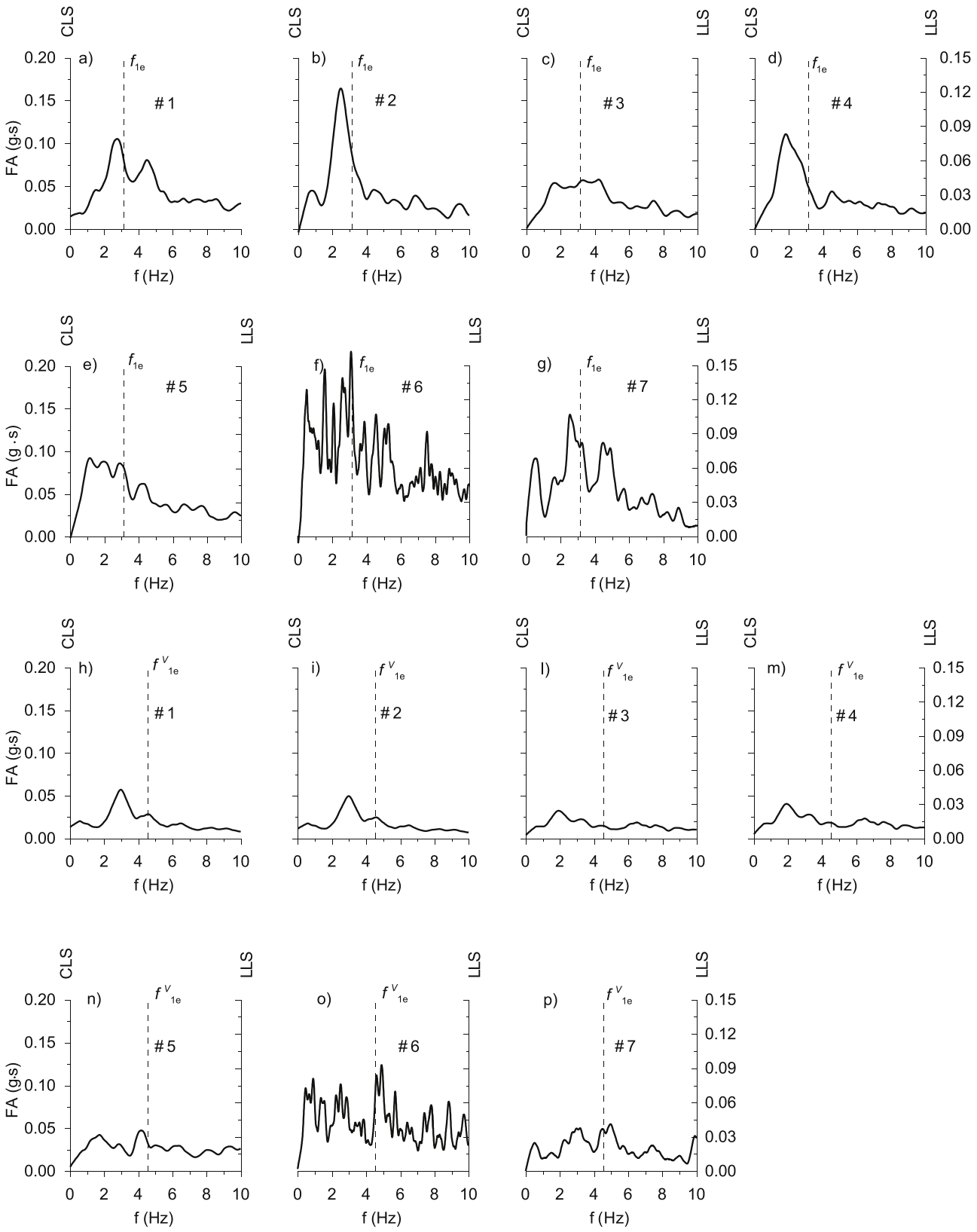

Fig. 5. Smoothed Fourier amplitude spectra of the horizontal (a–g) and vertical (h–p) components of the scaled seismic records.

For all the horizontal components of the scaled records, Fig. 6 provides the values of: the mean T_m [23] and the predominant T_p periods (Fig. 6 a,b) superimposed to the first natural period of horizontal elastic vibration of the dam $T_{1e} = 1/f_{1e} = 0.32$ s; the strong motion duration $D_{5\text{-}95}$ [24] and the equivalent number of loading cycles N_{eq} [25] (Fig. 6 c, d); the Arias intensity I_A [26] and the destructiveness potential factor P_d [27] (Fig. 6 e,f).

In the analyses, the seismic input was applied at the bottom of the

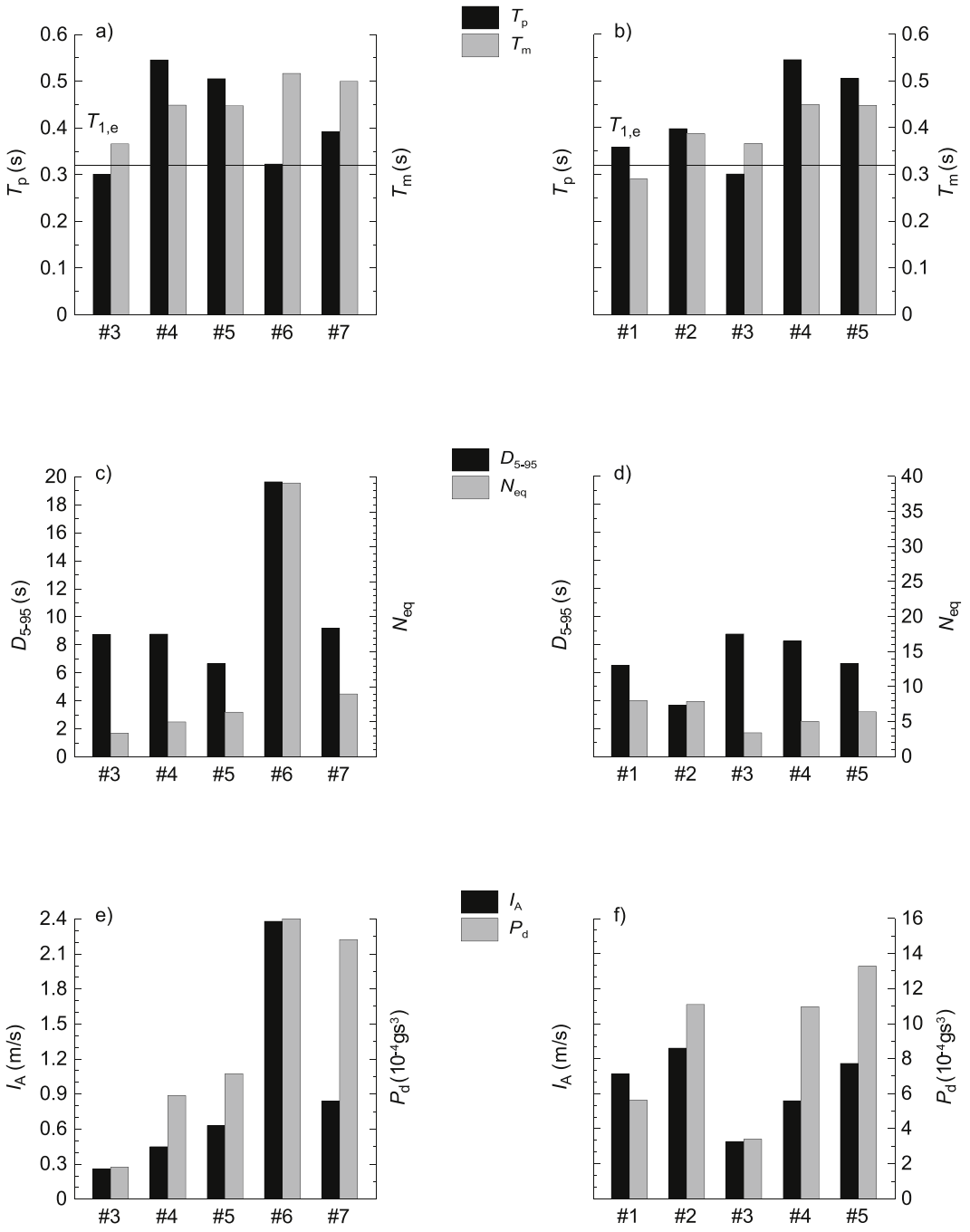

Fig. 6. Main seismic parameters of the horizontal component of the input motions selected and scaled for the *LLS* (a, c, e) and the *CLS* (b, d, f) analyses.

grid converting the horizontal and vertical time-histories of velocity associated to the corresponding acceleration records into shear and normal stress time-histories, as usual when using quiet boundaries (see § 2.1).

3. Preliminary dynamic analyses

For the seismic scenarios defined according to the latest *PSHA* available for the site of the San Pietro dam, the paper aims to assess the influence of the vertical component of ground motion and of the earthquake-induced pore water pressure build-up on the seismic performance of zoned earth dams.

To this purpose, a set of preliminary analyses was first carried out ignoring both the vertical component of ground motion and pore water pressure build up, using the results as a reference for the comparison with the dynamic analyses performed accounting for each effect separately (§ 4 and 5) or for both of them (§ 6).

The preliminary dynamic analyses showed that:

- records #2 and #5 (*CLS*) led to relevant non-linear effects with large plastic shear strains in the dam body and crest settlements, due to their large energy content, reflected in the values of I_A and P_d (Fig. 6 e, f), and to their frequency content, mainly concentrated in the range of frequencies relevant for the non-linear dam response (Fig. 5 b, e);
- records #6 ($T_p = 0.323$ s) and #7 ($T_p = 0.392$ s), characterised by predominant periods T_p close to T_{1e} (Fig. 6 a, b) and having the largest energy content (I_A) and destructiveness potential factor (P_d)

among those selected for the *LLS* (Fig. 6 e, f), are responsible for relevant effects of frequency coupling and led to the most critical crest settlements and acceleration amplification.

Based on these considerations, the preliminary analyses are presented and discussed herein giving greater emphasis to the results computed for records #6 and #5 for the *LLS* and the *CLS*, respectively.

3.1. Earthquake-induced shear strains and permanent displacements

For all the acceleration records selected for the analyses Table 3 (*CLS*) and 4 (*LLS*) list the maximum vertical and horizontal displacements computed in the dam at the end of seismic shaking; these values are provided for the upstream and downstream portions of the dam body as well as for its crest. Similarly, Fig. 7 shows the time-histories of the crest settlements (Fig. 7 a, d) together with the profiles, along the dam axis, of the vertical (Fig. 7 b, e) and horizontal (Fig. 7 c, f) displacements relative to the base of the dam computed at the end of the analysis; negative values indicate horizontal displacements directed upstream and vertical displacements directed downward.

As a general remark it can be observed that for both the considered limit states, the largest displacements are generally predicted in the upstream direction (Tables 3 and 4) and correspond to the input motions characterised by the largest energy content (I_A) and destructiveness potential (P_D) of the corresponding acceleration time-history. The highest crest settlement is equal to about 16 cm (Figs. 7 a) and 12 cm (Fig. 7 d) for the *LLS* (record #6) and the *CLS* (record #5), respectively.

Irrespective of the considered limit state and the adopted input motion, the vertical displacements decrease with depth with the highest gradients always localised in the upper third of the dam (Fig. 7 b, e). Also, in most cases the profiles of horizontal displacements (Fig. 7 c, f) exhibit larger values in the upstream directions with peaks at the crest level of about 10 cm (Figs. 7 c) and 21 cm (Fig. 7 f) for the *LLS* (record # 6) and the *CLS* (record #5), respectively.

For the most severe input motion selected for the *CLS* (record # 5) and *LLS* (record # 6), Fig. 8 shows the contour lines of vertical (Fig. 8 a, d) and horizontal (Fig. 8 b,e) permanent displacements and shear strains (Fig. 8 c,f) computed at the end of shaking. For the *CLS* (Table 3), the largest permanent displacements are equal to $u_h = 32$ cm (Fig. 8 a) and $u_v = 33$ cm (Fig. 8 b); values of the shear strains generally less than $\gamma = 4\%$ and locally up to 5% (Fig. 8 c) were also estimated; similarly, the corresponding largest displacement and shear strain computed for the *LLS* (Table 4) are $u_h = 43$ cm (Fig. 8 d), $u_v = 48$ cm (Fig. 8 e) and $\gamma = 5$–6% (Fig. 8 f).

In both cases, the horizontal displacements of the upstream shell are also of opposite sign to those computed for the downstream shell, showing a bulging of the dam during the seismic excitation. In Fig. 8 it is apparent that displacements develop in a shallow portion of the dam section, without affecting the core. This result is common to the whole set of the analyses and has a twofold remarkable implication. In fact, if the core does not suffer significant deformation, the hydraulic tightness of the dam will be preserved and no uncontrolled release of water will arise.

Table 3
Peak permanent displacements computed for the *CLS* at the crest and in the upstream and downstream portions of the dam including or ignoring the vertical component of input motion (a_v) and accounting or not for possible development of the pore water pressure build-up (Δu).

analysis			upstream		crest	downstream	
a_v	Δu	record	u_v (cm)	u_h (cm)	w_c (cm)	u_v (cm)	u_h (cm)
no	*no*	#1	−21	−14	−4.81	−4	11
		#2	−32	−25	−11.4	−10	19
		#3	−13	−12	−2.33	−2	6
		#4	−19	−17	−5.54	−6	15
		#5	−32	−33	−11.9	−8	12
yes	*no*	#1	−23	−18	−6.7	−6	12
		#2	−39	−28	−11.3	−10.3	19.2
		#3	−10	−12	−1.1	−2	5
		#4	−22	−18	−6.5	−11.5	20
		#5	−31.5	−30	−10.3	−8.2	12.4
no	*yes*	#1	−49	−54	−6.1	−7	13
		#2	−63	−68	−19.6	−12	19
		#3	−39	−51	−4.7	−2	6
		#4	−54	−67	−12.4	−9	14
		#5	−58.5	−80	−20.1	−13.5	12
yes	*yes*	#1	−64	−52.5	−15.2	−10	13
		#2	−70	−80	−22.5	−12.5	18
		#3	−31	−55	−3.42	−2	6.5
		#4	−55	−72	−12.9	−12	18
		#5	−61	−66	−22.4	−12	12.5

3.2. Acceleration amplification

For both the *LLS* and the *CLS* and for all the selected input motions, Fig. 9 shows the profiles of the maximum horizontal ($a_{h,max}$) and vertical ($a_{v,max}$) accelerations along the axis of the dam, normalised to the peak horizontal acceleration computed at its base $a_{h,base}$; the shaded area depicted in Fig. 9 a,c corresponds to the envelope provided by Aliberti et al. [28].

As far as the horizontal acceleration is concerned, a small amplification ratio $a_{h,max}/a_{h,base}$, always lower than 1.5, is generally observed in the profiles obtained for *CLS* (Fig. 9 c), while larger amplification ratios, up to 2.45, were evaluated for the *LLS* (Fig. 9 a). As expected, the larger accelerations of the input motions selected for the *CLS* led to larger deformations and energy dissipation, this inducing lower amplification peaks in the dam body.

The ratio $a_{v,max}/a_{h,base}$ (Fig. 9 b,d) is generally higher in the upper third of the dam, with values of $0.5 \div 2$ and $0.5 \div 1.5$ for the *LLS* (Fig. 9 b) and the *CLS* (Fig. 9 d), respectively. This points out the onset of a parasitic vertical component of the seismic acceleration generated by wave reflection phenomena that occur at the free surface of the dam and within the dam embankment.

The distribution of peak horizontal and vertical accelerations computed along the surface profile and at the base of the dam are shown in Fig. 10 with reference to records #5 and #6 selected for the *CLS* and *LLS*, respectively. The largest accelerations are reached on the surface of the dam as a result of both stratigraphic effects and amplification of ground motion due to focusing of the seismic waves induced by the interaction of the incident and reflected waves, that is highest close to the dam crest. Outside the dam body the peak accelerations reduce with the distance from the dam axis, until they are no longer affected by the topographic effects.

Fig. 10 a,c compares the computed values of peak horizontal acceleration $a_{h,max}$ with those evaluated through the simplified relationship indicated in the Italian seismic code [1]: $a_{h,max} = a_{g,T} \cdot S_T \cdot S_S$, using a topographic amplification factor $S_T = 1.2$ and a stratigraphic amplification factor S_S equal to 1.27 and 1.11 for the *LLS* ($a_{g,T} = 0.304g$) and *CLS* ($a_{g,T} = 0.414$).

The peak horizontal acceleration evaluated at the dam site ($a_{g,T} \cdot S_S$) is in a fair agreement with (*LLS* – Fig. 10 a) or slightly larger than (*CLS* – Fig. 10 c) that obtained in the dynamic analyses. Conversely, the numerical analyses provide horizontal accelerations at the dam crest and along the upper portions of the shells greater than those evaluated through the simplified estimate ($a_{g,T} \cdot S_T \cdot S_S$).

Fig. 10 a,c also shows the horizontal crest acceleration computed using the modified Makdisi & Seed [29] procedure proposed by Biondi et al. [3], $a_{max,\ crest} = 0.565g$ and $0.788g$, that are in a good agreement with results of the dynamic analyses.

The peak vertical acceleration (Fig. 10 b,d) computed along the profile of the dam are compared to the anchor value $a_{g,v}$ of the elastic

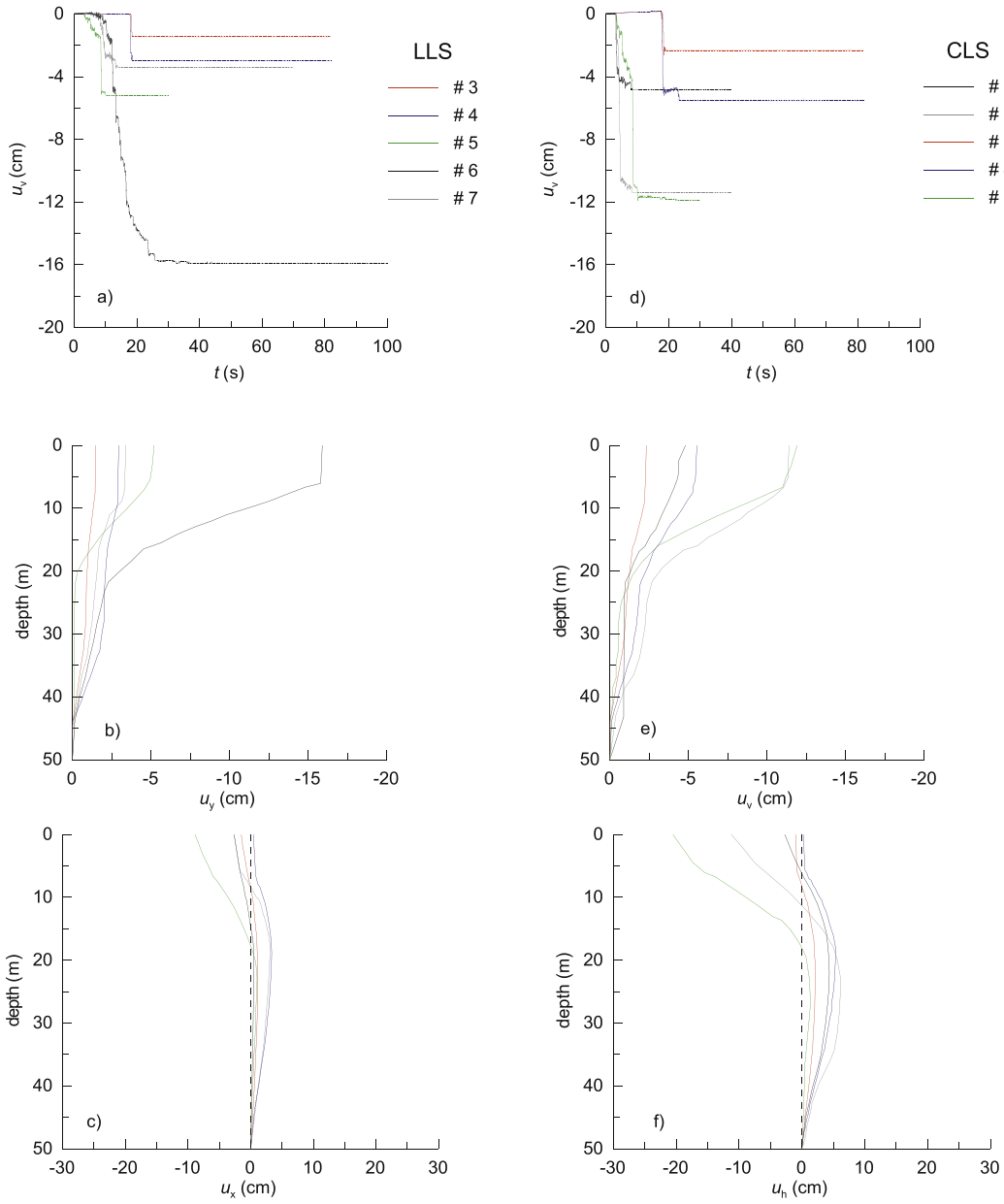

Fig. 7. Time histories of crest settlement (a, d) and profiles along the dam centre line of the vertical (b, e) and horizontal (c, f) displacements relative to the base, computed for the *LLS* (record #6) and *CLS* (record #5) accounting for the horizontal input motion only and ignoring pore water pressure build-up.

response spectrum defined by NTC18 [1] for the vertical acceleration, using a topographic factor $S_T = 1.2$. The simplified estimate overpredicts the parasitic vertical acceleration in the soil volumes aside the dam but generally provides an underestimate in the dam body, especially close to the crest.

4. Influence of vertical component of input motion

The analyses presented in the previous section were repeated accounting for the vertical component of the input motions. The vertical and horizontal displacements computed at the end of seismic shaking are listed in Table 3 (*CLS*) and 4 (*LLS*) showing that the influence of the vertical component of input motion is comparable for both the *CLS* and *LLS*.

Compared with the displacements discussed in the previous section (§ 3), accounting for the vertical component of ground motion results in a not definite influence on the permanent displacements.

In fact, for the *CLS* analyses, depending on the considered input motion, vertical displacements decrease up to 23% (record #3), increase up to 92% (record #4) or remain approximately unchanged (records #2 and #5); anyway, when a remarkable change in vertical displacements is observed, the absolute values are relatively small, increasing, in the worst case (record #4), from 6 cm to 11.5 cm. Similarly, increments up to 33% (record #4) and reductions up to 17% (record #3) are observed for the horizontal displacements, even if in most cases the displacements remain nearly unchanged, thus suggesting a limited effect of the vertical component of ground motion for the horizontal displacements too.

Also for the *LLS* the introduction of the vertical component of the input motion produced different variations depending on the considered input motion. As an example, vertical displacements decrease up to 18% (record #5), increase up to 167% (record #5) or remain approximately unchanged (record #3) and, again, remarkable changes occur in the case of relatively small displacements.

As shown in Tables 3 and 4, even when considering the vertical component of input motion, records #2 and #5 and records #6 and #7 are the most severe for the *CLS* and *LLS* analyses, respectively. The

Table 4
Peak permanent displacements computed for the *LLS* at the crest and in the upstream and downstream portions of the dam including or ignoring the vertical component of input motion (a_v) and accounting or not for possible development of the pore water pressure build-up (Δu).

analysis			upstream		crest	downstream	
a_v	Δu	record	u_v (cm)	u_h (cm)	w_c (cm)	u_v (cm)	u_h (cm)
no	*no*	#3	−6.5	−7.5	−1.45	−1	2.5
		#4	−12.5	−11	−2.96	−3	7
		#5	−22	−19	−5.19	−3	7
		#6	−43	−48	−15.9	−14	23
		#7	−25	−30	−3.4	−2	−7
yes	*no*	#3	−6	−7	−1	−1	2
		#4	−13	−9	−2	−4	10
		#5	−18	−18	−4.2	−8	9
		#6	−63	−48	−25.1	−34	37
		#7	−26	−29	−4	−3	7
no	*yes*	#3	−22	−39	−2.4	−1	3
		#4	−32	−43	−6.2	−4	8
		#5	−41	−56	−12.3	−7	7
		#6	−84	−131	−39.1	−26	28
		#7	−51	−71	−9.8	−3	6
yes	*yes*	#3	−17	−38	−1.7	−1.5	2
		#4	−33	−43	−7.4	−4	9
		#5	−39	−51	−9.2	−5	7
		#6	−101	−129	−46.2	−52	39
		#7	−53	−82	−9	−5	7

results computed using these records, are presented in Fig. 11 in terms of the time histories of crest settlements (Fig. 11 a, b), profiles of the normalised peak horizontal ($a_{h,max}/a_{h,base}$, Fig. 11 c, d) and vertical ($a_{h,max}/a_{h,base}$, Fig. 11 e, f) accelerations. The results computed ignoring the vertical component of ground motion (§ 3) are also plotted in the figures for comparison.

Despite significant differences can be observed in the time histories of crest settlements (Fig. 11 a, b), that exhibit instantaneous spikes when vertical acceleration is input in the model, the influence of the vertical component of ground motion is hardly appreciable on the final values of the vertical displacement of the dam crest computed for the *CLS* while is noticeable in the case of the record #6 selected for the *LLS* analyses.

Also, the horizontal amplification pattern of the dam, represented by the *in-axis* profiles of Fig. 11 c-d, appears to be only slightly affected by the vertical component of ground motion.

Comparing the permanent displacements listed in Tables 3 and 4 and plotted for the record #5 (*CLS*) in Fig. 12 a,c,e and 8 a,c,e, accounting or neglecting the vertical component of ground motion, it is apparent that this result can be extended to the overall embankment and can be ascribed to the circumstance that the predominant frequencies of most of the considered vertical input motions (Fig. 5 h-p) are far from the first natural frequency of vertical ($f^v_{1e} = 4.54$ Hz) elastic vibration of the dam.

Accordingly, as also reported in the literature (e.g. Ref. [30]), the overall negligible effect of the vertical input motion on the acceleration and displacement fields of an earth dam cannot be considered as a general result and is generally related to the amplitude and the frequency content of the seismic motion (e.g. Ref. [31]) and to the possible coupling between the frequency content of the vertical component of the input motion and the natural frequencies of vertical elastic vibration of the dam.

For the case at hand the amplitude (Fig. 4 h-p) and frequency (Fig. 5 h-p) content of the vertical component of the selected input motions do not affect significantly the response of the dam since: *i*) the ratio ($a_{v,max}/a_{h,max}$) of the vertical to horizontal peak accelerations is always limited in the range 0.30 ÷ 0.61 (with the only exception of record #6 for which is $a_{v,max}/a_{h,max} = 0.91$); *ii*) despite the short site-to-source distances ($R_{jb} = 4.66 \div 15.58$ km, Table 2), the motion expected at the dam site is not dominated by the vertical component at high frequencies; *iii*) the predominant frequencies of the vertical input motions (which are mainly concentrated in the same range of frequencies relevant for the larger horizontal components) are generally lower than f^v_{1e} (with the only exception of record #6) and thus the horizontal input motions, approximately coupled with f_{1e} (Fig. 5 a-g), mainly control the seismic dam response. Conversely, in the case of the record #6 (Fig. 8 a,c,e and Fig. 12 a,c,e), for which a frequency coupling occurs between the vertical input acceleration and f^v_{1e} (Fig. 5 o), the effect of the vertical component is relevant due to the large vertical to horizontal peak acceleration ratio ($a_{v,max}/a_{h,max} = 0.91$) and to the closeness between the predominant frequencies of the vertical motion and the first natural frequency of vertical elastic vibration of the dam f^v_{1e} (Fig. 5 o). Accordingly, increments in the vertical displacements of about 47% and 58% in the upstream shell and at the crest, respectively, and even larger in the downstream shell are obtained.

5. Influence of excess pore water pressure

Numerical analyses accounting for pore water pressure build-up were carried out to check the occurrence of shear strength reduction in the soils of the dam. These analyses were inspired by the relatively low values of penetration resistance measured by the SPT tests in the shallowest portion of the coarse-grained soil of the shells.

Accordingly, for all the records selected for the *LLS* and the *CLS*, the FD analyses were repeated accounting for the possible occurrence of excess pore water pressure. To focus this effect only, the vertical component of ground motion was ignored in these analyses whose results are discussed in terms of earthquake-induced shear strains, permanent displacements and acceleration amplification in the dam body.

5.1. Earthquake-induced shear strains and permanent displacements

Tables 3 and 4 list the values of the vertical and horizontal permanent displacements predicted at the end of shaking in the downstream and upstream portions and at the crest of the dam for all the input motions selected for the *CLS* and the *LLS*. Again, records #2 and #5 for the *CLS* and records #6 and #7 for the *LLS* led to the largest permanent displacements. These were predicted in the upstream shell with maximum horizontal and vertical components equal to 80 cm (#5) and 63 cm (#2), respectively for the *CLS* (Table 3) and to 131 cm (#6) and 84 cm (#6), for the *LLS* (Table 4).

The comparison with the results obtained ignoring the occurrence of excess pore water pressure (Tables 3 and 4), shows that, as expected, an increase in excess pore water pressures mainly affect the upstream side of the dam, leading to horizontal and vertical displacements that are two-to-four and two-to-three times larger, respectively.

These results can be related to the reduction of the effective state of stress and as shown later, to the development of deeper and longer shear bands in the upstream shell of the dam.

As an example, Fig. 13 shows the contours of vertical and horizontal components of permanent displacements (Fig. 13 a-d), shear strain (Fig. 13 e,f) and excess pore water pressure Δu (Fig. 13 g,h - positive Δu means an increase of u relative to its initial value) induced by records #5 for the *CLS* and #6 for the *LLS*. These results can be compared with those shown in Fig. 8 using the same records but ignoring the occurrence of pore water pressure build-up.

It is apparent an enlargement of the portion of the dam section for which high shear strains are computed and a general increase of their values (Fig. 8 e,f and 13 e,f). High shear strains are attained in a narrow band, along a surface that encompasses the shallow portion of the upstream shell (Fig. 13 e,f), thus detecting a plastic mechanism that is temporarily activated by the earthquake. Increments in the earthquake-induced shear strains due to the increase in pore water pressure are also computed in the core (Fig. 13 g,h), which however is not involved in the

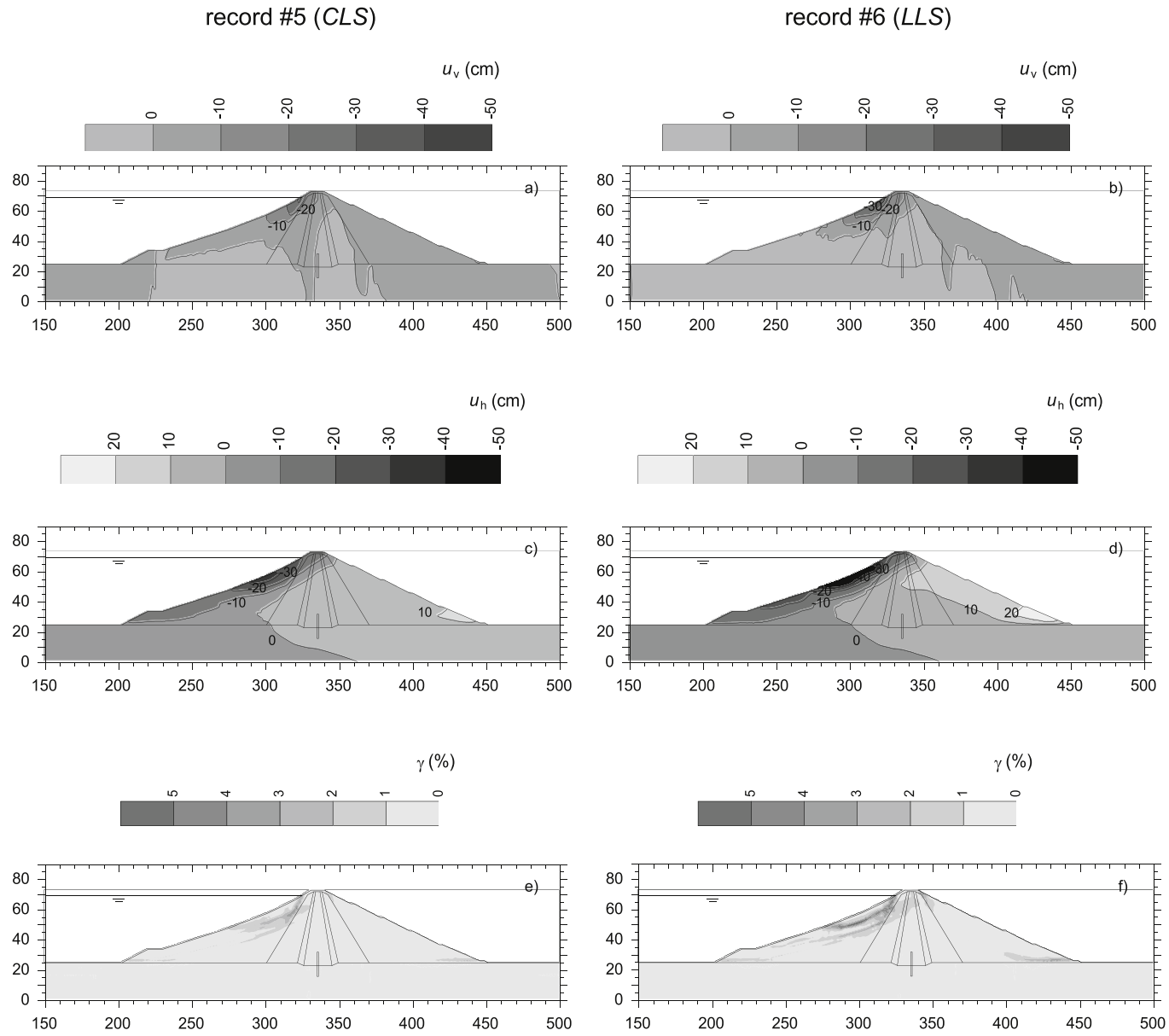

Fig. 8. Contours of vertical (a,b) and horizontal (c,d) permanent displacements and shear strains (e,f) computed for record #5 (a, c, e) selected for the *CLS* and for record #6 (b, d, f) selected for the *LLS* accounting only for the horizontal input motion and ignoring pore water pressure build-up.

plastic mechanism.

Increments in the permanent displacements can be also observed comparing the contours of the vertical (Fig. 8 a,b and 13 a,b) and horizontal (Fig. 8 c,d and 13 c,d) components of displacements. The observed differences can be ascribed to the occurrence of pore water pressure build-up in the upstream shell, in the core and in the portion of the downstream shell located underneath the water table (Fig. 13 g,h). Instead, as eexpected, the overall effect of pore pressure build-up on the displacement field computed in the downstream side of the dam is moderate (Fig. 13 g,h).

5.2. Acceleration amplification

For records #2 and #5 of the *CLS* and #6 and #7 of the *LLS*, Fig. 14 shows the time histories of crest settlements (Fig. 14 a, b), the crest-to-base amplification functions (Fig. 14 c, d) and the profiles of the normalised horizontal acceleration computed along the centre line of the dam section (Fig. 14 e, f); the results computed for the same limit state and input motions, but ignoring the occurrence of pore pressure build-up (§ 3) are also plotted for comparison in the figures.

As a consequence of the pore pressure build-up, increments in the permanent crest settlement of about 70% for records #5 and #2 (*CLS*, Fig. 14 a; Table 3) and up to 150%–200% for the records #6 and #7 (*LLS*, Fig. 14 b; Table 4) are predicted and the largest crest settlements are of about 20 cm (#5) and 40 cm (#6).

The computed time-histories (Fig. 14 a, b) show that the more relevant differences are due to the instantaneous increments occurring at the sharpest peaks of the horizontal acceleration time-histories (Fig. 4 b,c).

Due to the weakening effects associated to the pore water pressure build-up, larger plastic strains arise in the dam body causing a greater energy dissipation.

As a consequence, for the considered input motions, smaller amplitudes of most ot the peaks of the amplification functions (Fig. 14 c, d) are generally computed when accounting for pore water pressure build-up, this leading to a lower amplification of the horizontal accelerations in the dam.

Accordingly, lower amplifications in the upper third of the dam can be observed in the profiles of Fig. 14 e, f computed accounting for excess

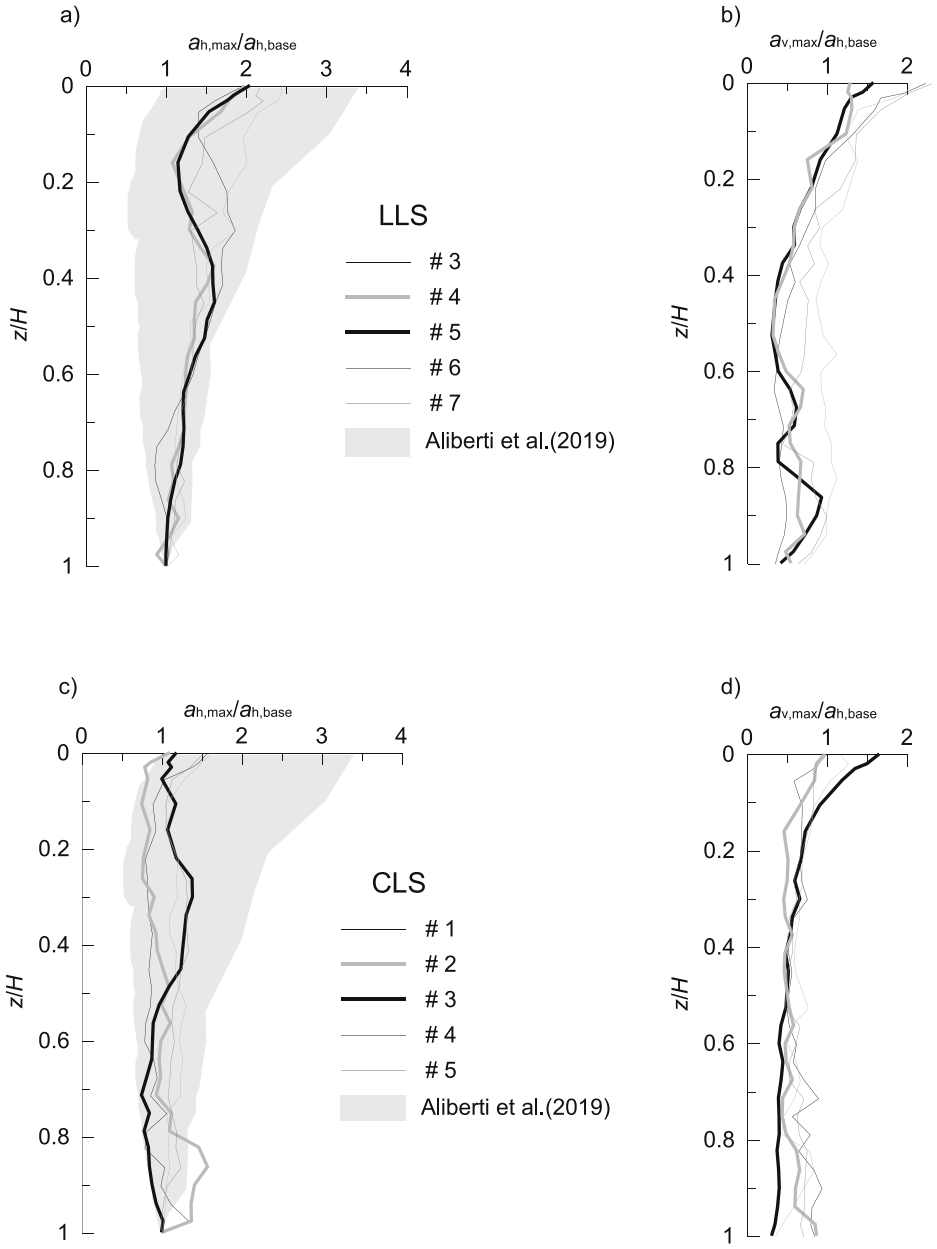

Fig. 9. Profiles of the normalised horizontal (a, c) and vertical (b, d) accelerations computed for the *LLS* (a, b) and *CLS* (c, d) accounting for the horizontal input motion only and ignoring pore water pressure build-up.

pore water pressures. The amplification ratio at the crest reduces from 1.1 to about 0.75 for record #5 and from 1.6 to about 0.65 for record #2 of the *CLS* and from 2.2 to about 1.2 for record #6 and from 2.4 to about 2.2 for record #7 of the *LLS*.

6. Combined influence of vertical input motion and excess pore pressures

The seismic performance of the dam was evaluated through a set of dynamic analyses carried out accounting for both the possible development of excess pore water pressure and the vertical component of input motion.

The analyses were performed for all the input motions selected for the *LLS* and *CLS* and the results are presented focusing on the main features of dam response which are discussed in terms of earthquake-induced plastic mechanism and corresponding permanent displacement of the dam body.

Also, the significant role of the energy content of input motion and of the combined effect of frequency coupling and non-linear soil behaviour is analyses with reference to the whole sets of input motion selected for both the considered limit states.

6.1. Earthquake-induced plastic mechanisms

Fig. 15 shows the contours of vertical and horizontal components of permanent displacement (Fig. 15 a-d), shear strain (Fig. 15 e,f) and excess pore water pressure ratio $\Delta u^* = \Delta u/\sigma'_{v0}$ (Fig. 15 g,h) computed using record #5 for the *CLS* and record#6 for the *LLS* as input motion.

The inspection of the contours and the comparison with those computed in the preliminary set of dynamic analyses (§ 3, Fig. 8) permit to evaluate the combined effect of pore water pressure build-up and vertical component of input motion.

The contours of vertical (Fig. 8 a,b and 15 a,b) and horizontal (Fig. 8 c,d and 15 c,d) permanent displacements show that most of the

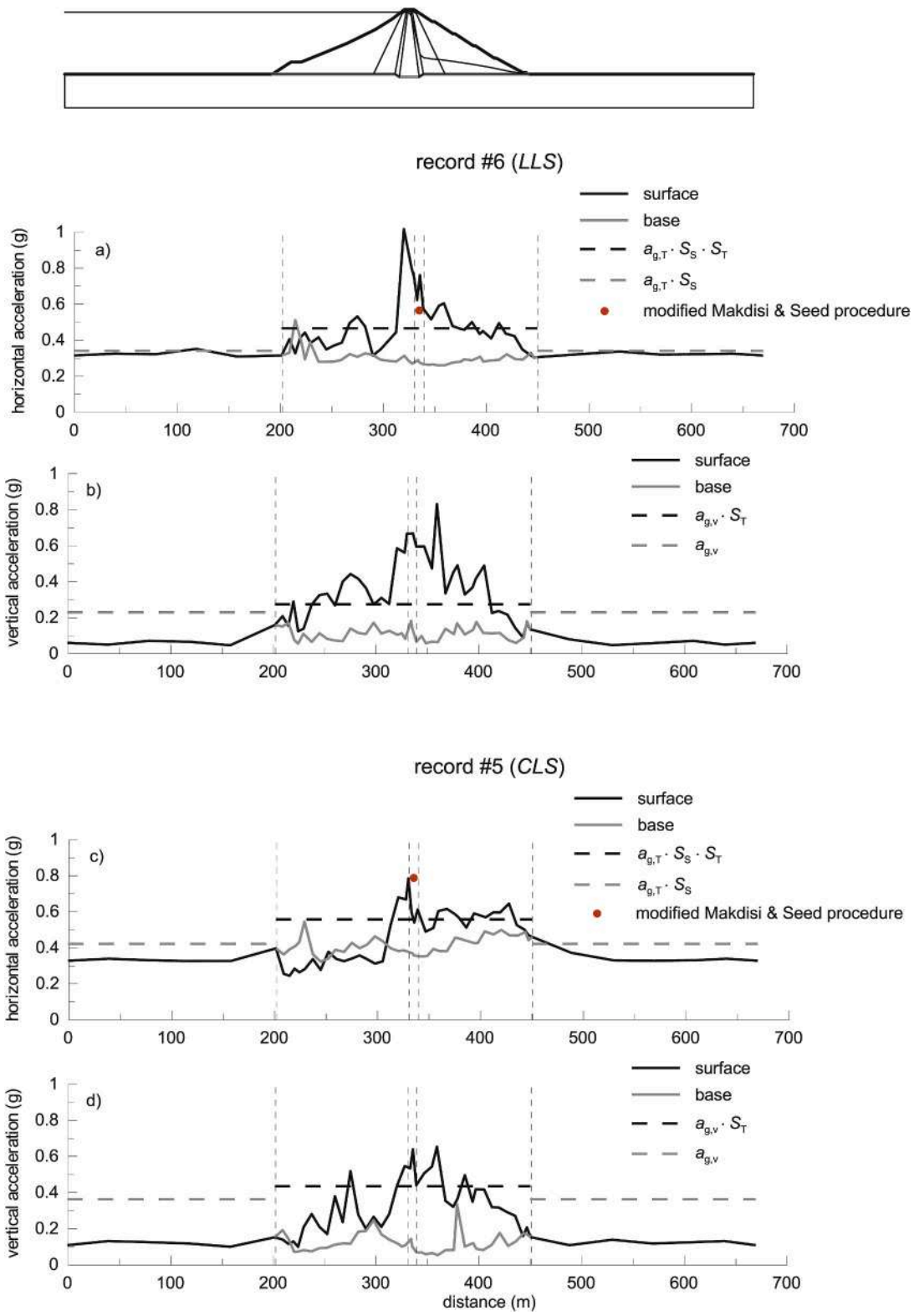

Fig. 10. Horizontal (a, c) and vertical (b, d) accelerations along the surface profile and at the base of the dam, for the *LLS* (record #6) and *CLS* (record #5), accounting for the horizontal input motion only and ignoring pore water pressure build-up.

displacement increments occur in the upstream shell, where peak shear strains are generally higher than 3%, and up to 7% for the record #5 (Fig. 15 e) and generally higher than 5%, and up to 12% for the record #6 (Fig. 15 f). Shear strains localisation attained along narrow bands indicates temporary activations of plastic mechanisms, associated to transient mobilisation of the shear strength, deeper than those computed in the reference analyses (Fig. 8 e,f) and extending from the crest to the toe of the upstream shell.

Large plastic strains result in higher excess pore pressure Δu arising in the upstream shell, in the core and in the lower portion of the downstream shell. The contours of Fig. 15 g,h show that the largest values of Δu^* are predicted in the lower portion of the shells where, due

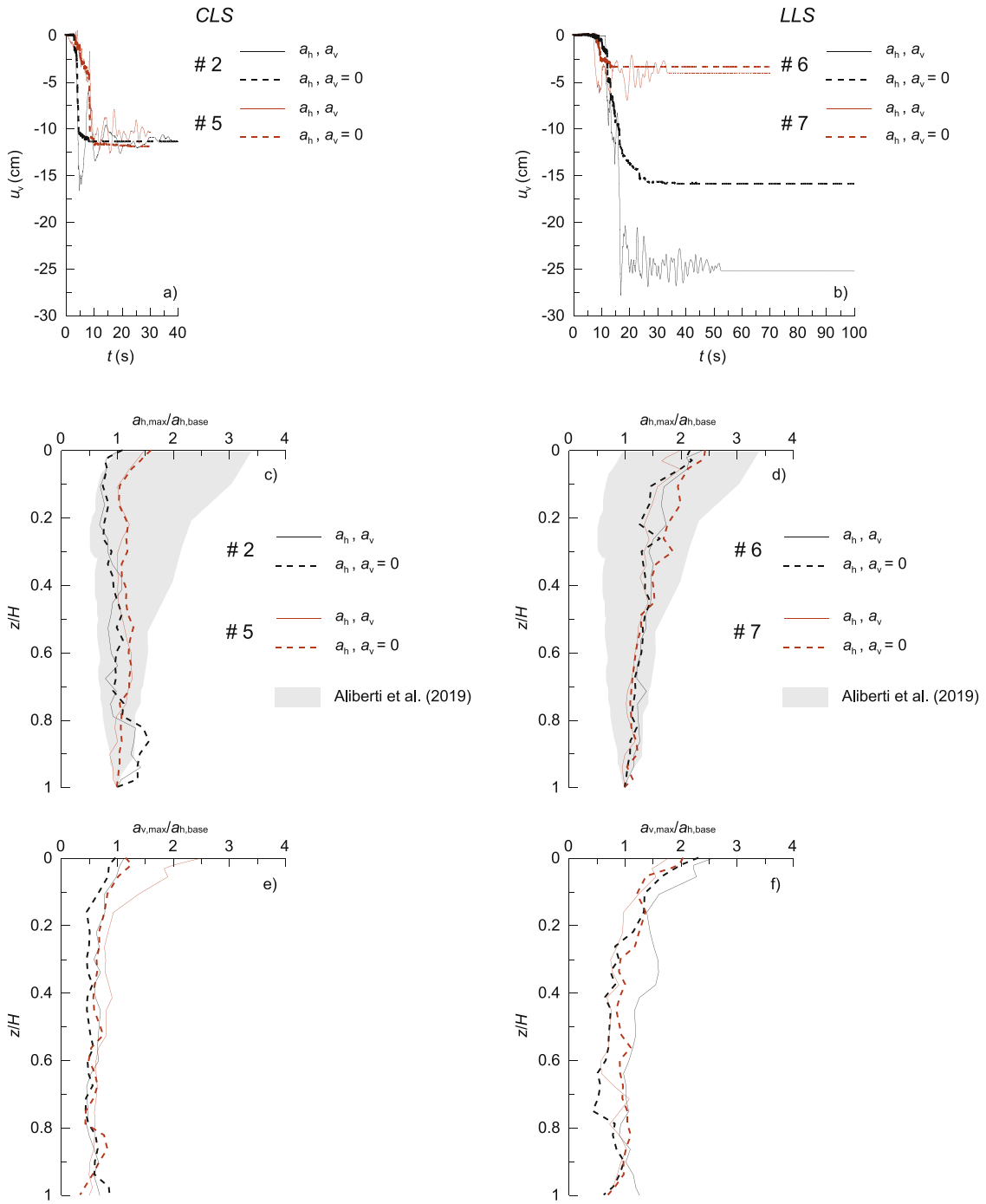

Fig. 11. Influence of the vertical input motion computed for records #2 and #5 (a, c, e) selected for the *CLS*, for records #6 and #7 (b, d, f) selected for the *LLS*: a, b) time-histories of crest settlement; c, d, e, f) profiles of horizontal (c,d) and vertical (e,f) normalised accelerations along the dam centre line.

to the higher effective stresses, the soil response to cyclic loading is characterised by a contracting behaviour; conversely, tendency of the shallower portions of the shells to dilate, leads to negligible excess pore water pressure.

Peak values of the excess pore water pressure ratio $\Delta u^* = 0.2$ to 0.7 (Fig. 15 g,h) are predicted along the shear bands observed in the contours of the peak shear strains (Fig. 15 e,f). In all the examined cases, the computed values of Δu^* are not large enough to compromise overall stability of the dam. Accordingly, the seismic performance of the dam should be evaluated in terms of admissibility of the permanent displacements induced by earthquake loading.

6.2. Permanent displacements

Fig. 16 summarises the results of the analyses performed for the *CLS* accounting for the possible occurrence of excess pore pressure and for the vertical component of the input motion. They are presented in terms of peak vertical and horizontal components of the permanent displacements computed in the upstream (Fig. 16 a, b) and downstream (Fig. 16 c, d) shells of the dam and are also listed in Table 3.

The vertical and horizontal displacements are in the ranges of 2–12 cm and 6–18 cm, respectively, for the downstream shell, while higher vertical and horizontal displacements are computed for the upstream shell, of 31–70 cm and 52–80 cm.

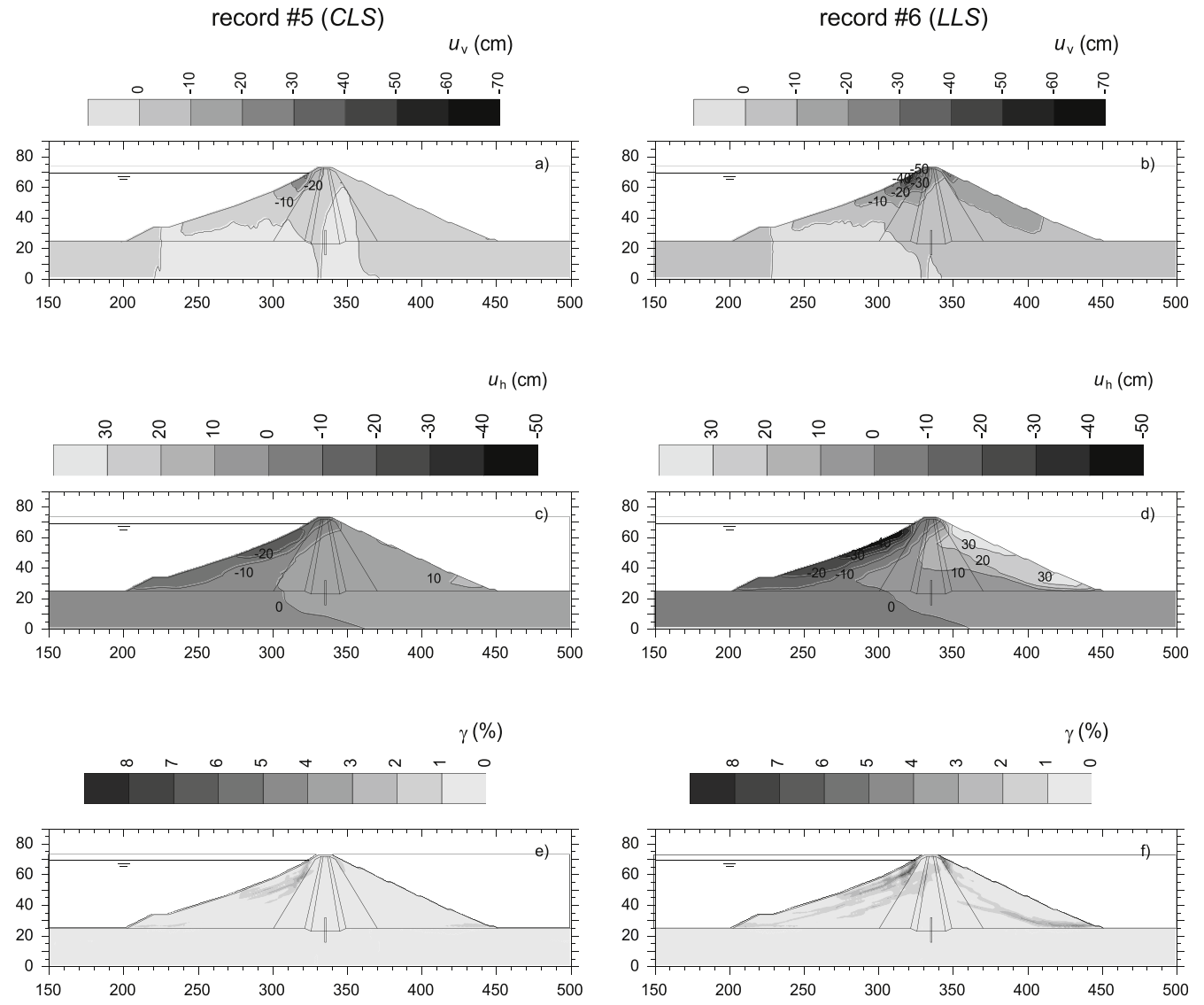

Fig. 12. Contours of vertical (a,b) and horizontal (c,d) permanent displacements and shear strain (e,f) computed for record #5 (*CLS* a,c,e) and record #6 (*LLS* b,d,f) accounting for the horizontal and vertical components of the input motion and ignoring pore water pressure build-up.

Remarkable increments are thus observed with respect to the reference analysis carried out ignoring pore water pressure build-up and the vertical component of ground motion (§ 3). The higher increments affect the upstream shell for which the vertical and horizontal permanent displacements are two-to-three and two-to-four times larger than those evaluated in the reference analyses.

The computed displacement are clearly related to the energy content and the destructiveness potential of the input motions: specifically, records #2 and #5, characterised by the largest values of I_A and P_d, provide the most severe effects in terms of pore water pressure build-up, leading to the highest vertical and horizontal displacements in the upstream shell. Similar response is detected comparing the time-histories of the crest settlements plotted in Fig. 17, accounting for (Δu, a_v) or ignoring ($\Delta u = 0$, $a_v = 0$) the influence of excess pore water pressure and vertical input motion: the highest crest settlement computed using records #2 and #5 is equal to about 22 cm, that is more than twice the values computed in the reference analyses ($\Delta u = 0$, $a_v = 0$).

As already discussed, the vertical component of input motion has not a definite effect on the magnitude of permanent displacements even when accounting for possible development of Δu during seismic shaking. As an example, depending on the considered input motion, increments of about 30–40% and reductions of about 10–20% can be observed for the vertical displacements (Table 3).

The results computed in the preliminary screening-level analyses [3] are also plotted in Fig. 16: these are the vertical and horizontal displacements computed through the original and the modified Makdisi & Seed procedure, through the empirical relationships proposed with reference to Italian seismicity [32,33], and using the other relationships adopted in the screening-level analyses (grey bars) performed for the San Pietro dam [3].

Regardless the considered input motion, the dynamic analyses always predict higher horizontal and vertical permanent displacements in the upstream shell of the dam, records #2 and #5 resulting the most severe seismic inputs for the collapse limit state (Fig. 16 a, b). Conversely, the simplified approaches adopted in the screening-level analyses prevalently overestimate horizontal and vertical displacements of the downstream of the dam (Fig. 16 c,d). For this shell, however, a fair prediction of displacement is achieved when using the modified Makdisi & Seed procedure and, to a less extent, the Rampello et al. [32] equation.

Simplified displacement analyses (e.g. Refs. [4,34]) are widely adopted for preliminary assessment of the dam seismic performance. However, in some cases they underestimate displacements observed in documented case-histories (e.g. Ref. [35]) or computed through

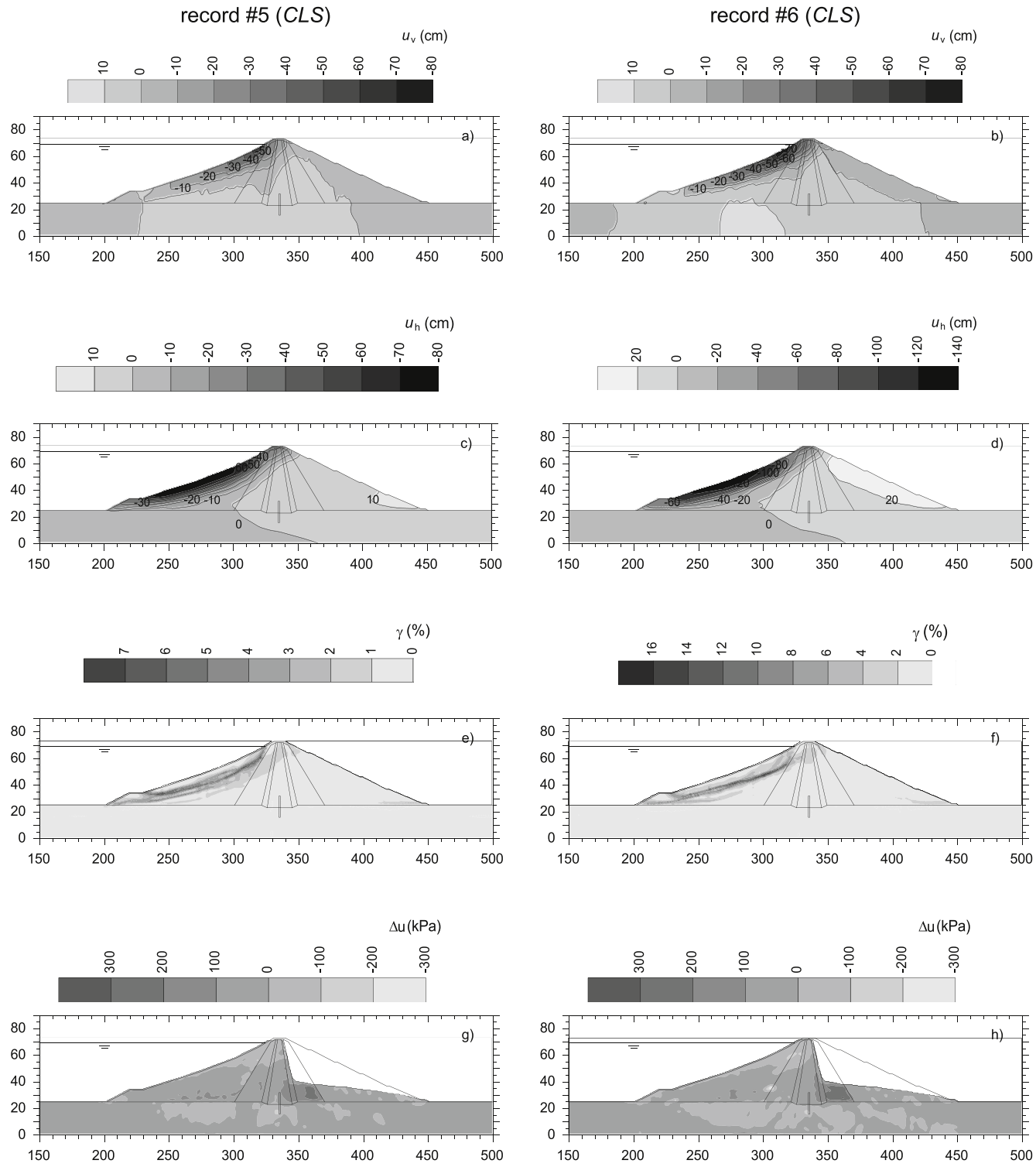

Fig. 13. Contours of vertical (a,b) and horizontal (c,d) permanent displacements, shear strain (e,f) and excess pore water pressure (g,h) computed for record #5 (*CLS* a,c,e,g) and record #6 (*LLS* b,d,f,h) accounting for the horizontal input motion only.

advanced numerical analyses. Differences in results provided by dynamic analyses and simplified displacement analyses may be ascribed to the fact that the latter do not represent properly the combined effects of cyclic soil behaviour and non-linear frequency coupling, that mainly rules the seismic dam performance, as shown in the following.

6.3. *Influence of energy content of the seismic input*

The crest settlement w_c (i.e. the vertical displacement u_v of the crest) computed accounting for (Δu, a_v) or ignoring ($\Delta u = 0$, $a_v = 0$) the influence of excess pore water pressure and vertical input motion are listed in Table 3 (*CLS*) and 4 (*LLS*) and are plotted in Fig. 18 versus the Arias intensity I_A (Fig. 18 a), the destructiveness potential factor P_d (Fig. 18 b) and the strong motion duration $D_{5\text{-}95}$ (Fig. 18 c) of the input motions. In

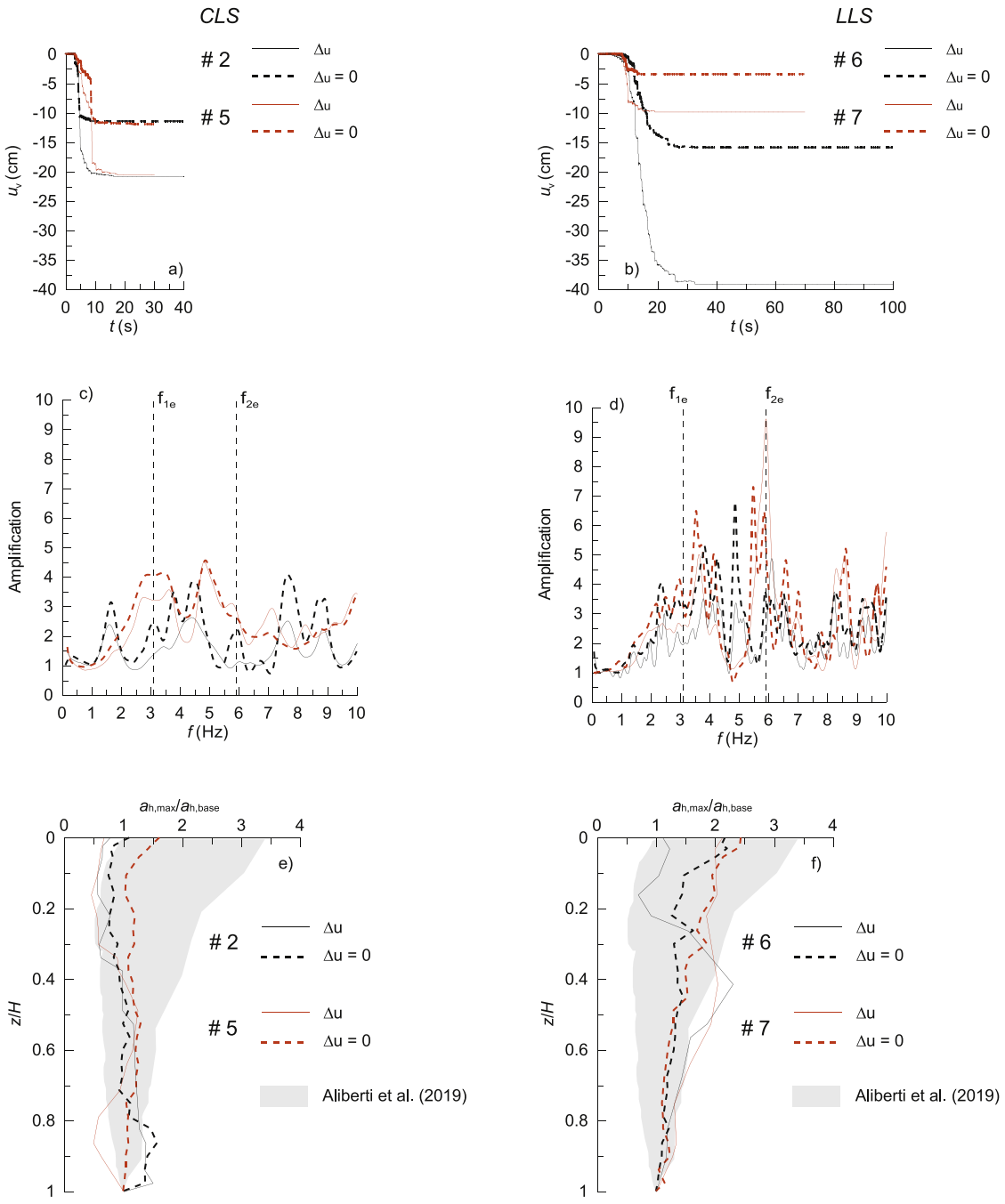

Fig. 14. Influence of the pore water pressure build-up computed for records #2 and #5 (a, c, e) , selected for the *CLS*, and for records #6 and #7 (b, d, e) selected for the *LLS*; a, b) time-histories of crest settlement; c, d) crest-to-base amplification functions; e) profiles of normalised horizontal acceleration along the dam centre line.

the evaluation of P_d, to avoid including zero crossings characterised by acceleration amplitude ineffective on the dam response, the frequency of zero crossings ν_0 was evaluated counting the number of zero crossings only in the duration $D_{5\text{-}95}$.

Fig. 18a also plots some empirical $w_c - I_A$ relationships derived for Italian dams: specifically, the linear relationship proposed by Pagano & Sica [36] for the Camastra dam, the envelopes of the $w_c - I_A$ pairs computed by Brigante & Sica [37] (data limited to $I_A \leq 4$ m/s) for the Conza Dam and those by Lanzo et al. [38,39] for the Licodia Eubea and Montedoglio dams. The figure shows that, with the exception of some data related to the *LLS* (record #6) and the *CLS* (records #2 and #5) analyses, the results of this study are in a fair agreement with those obtained for other Italian earth dams (Camastra, Conza and Montedoglio dams) and, as expected, differ from those obtained for the stiffer concrete gravity dam of Licodia Eubea.

Despite the high peak acceleration of the input motions selected for the *CLS* ($a_g = 0.414g$), and regardless the effect of pore water pressure build-up, the highest crest settlements were always predicted using record #6 selected for the *LLS* ($a_g = 0.304g$). Among the selected motions, record #6 is in fact characterised by the largest energy content, reflected in the highest values of I_A and P_d, and by a predominant period ($T_p = 0.323$ s) nearly coincident with the natural period of horizontal elastic vibration of the dam, this implying a frequency content concentrated in the range of frequencies relevant for the non-linear response of the dam.

Irrespective of the presence of the vertical component of input motion, the analyses that account for pore water pressure build-up confirm that w_c increases with I_A and a nearly linear upper-bound $w_c - I_A$ relationship (blu dashed line in Fig. 18 a) can be derived for the San Pietro

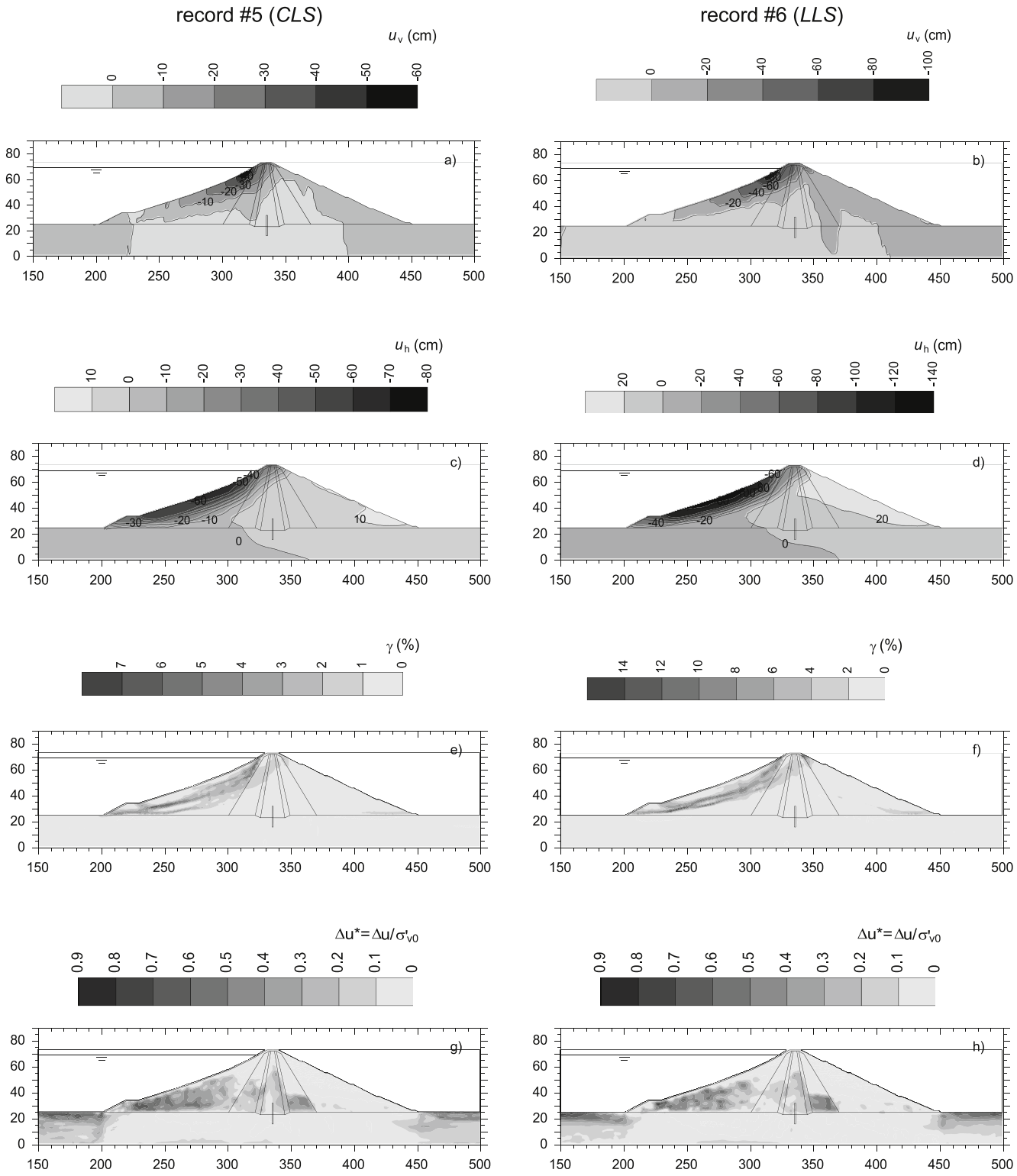

Fig. 15. Contours of vertical (a,b) and horizontal (c,d) permanent displacements, shear strain (e,f) and excess pore water pressure ratio (g,h) computed for record #5 (*CLS* - a,c,e,g) and record #6 (*LLS* - b,d,f,h) accounting for the vertical component of input motion.

dam and adopted for a safe evaluation of earthquake-induced crest settlements.

The relationship w_c – P_d shown in Fig. 18 b exhibits an increasing trend but is characterised by a larger scatter in comparison with the w_c – I_A relationship (Fig. 18 a).

Conversely, for the case at hand, the crest settlement reduces as the strong motion duration of the input motion increases (Fig. 18 c); this unexpected result is a consequence of the smaller Arias intensity and destructiveness potential factor of the input motions characterised by larger $D_{5\text{-}95}$ (Fig. 6). Strong motion duration produces indeed an increase of earthquake-induced displacements for seismic events strong enough to induce the activation of transient plastic mechanisms.

On the whole, consistently with Pagano & Sica [36] and Lanzo et al. [39], the computed results confirm that peak parameters of input

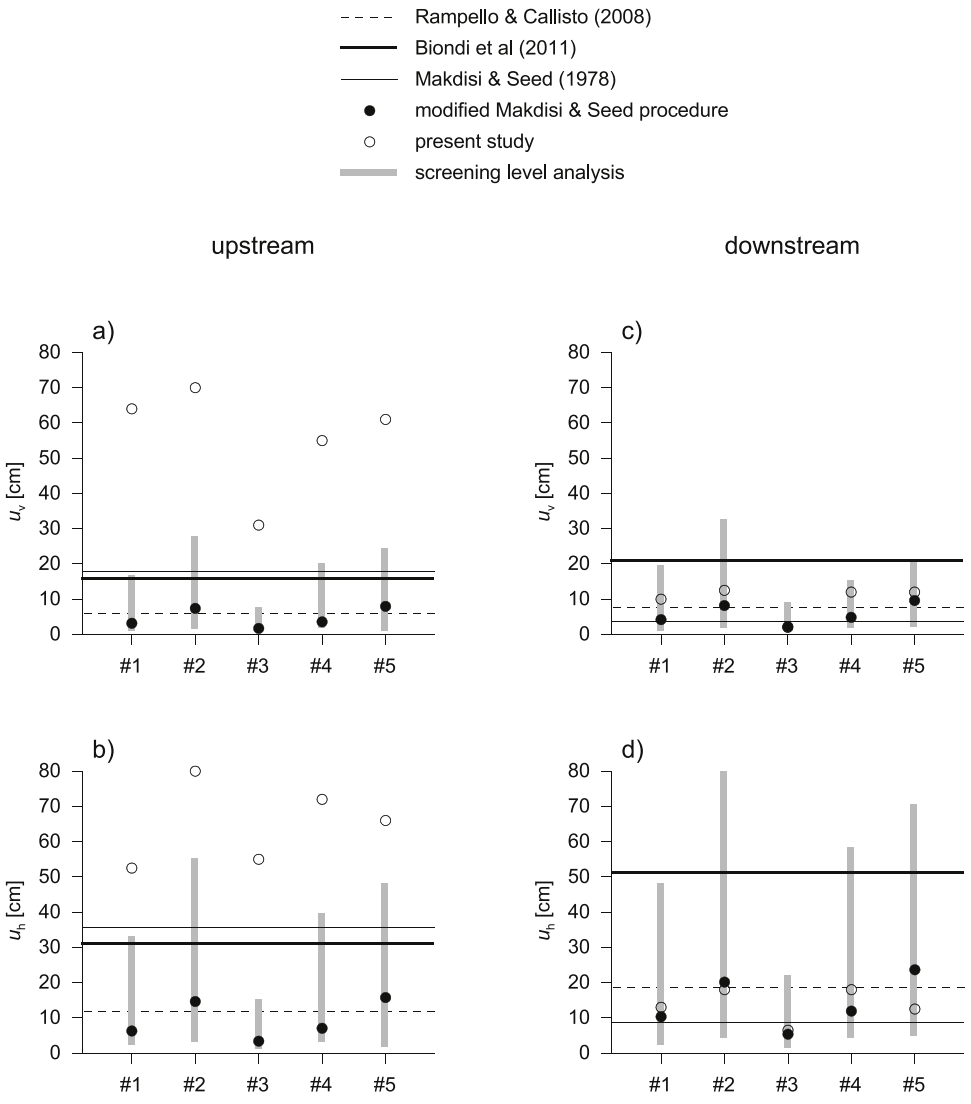

Fig. 16. Vertical (a,c) and horizontal (b,d) permanent displacements of the upstream (a,b) and downstream (c,d) shells computed for the *CLS* and comparison with the results of the screening-level analyses.

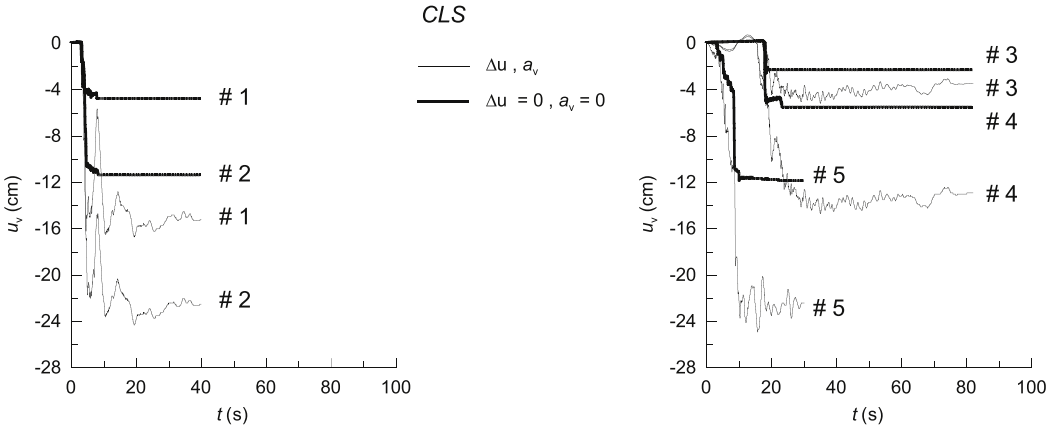

Fig. 17. Time histories of crest settlements computed for the records selected for the *CLS* neglecting ($\Delta u = 0$, $a_v = 0$) or accounting for (Δu, a_v) the combined effect of the excess pore water pressure and vertical input motion.

motions cannot be used for a safe assessment of the dam response, while, the Arias intensity, that accounts for the amplitude, duration and frequency content of the input motion, provide an adequate representation of the potential damage induced in the dam.

In fact, despite all the selected (scaled) input motions are characterised by the same peak horizontal acceleration, the scatter in the

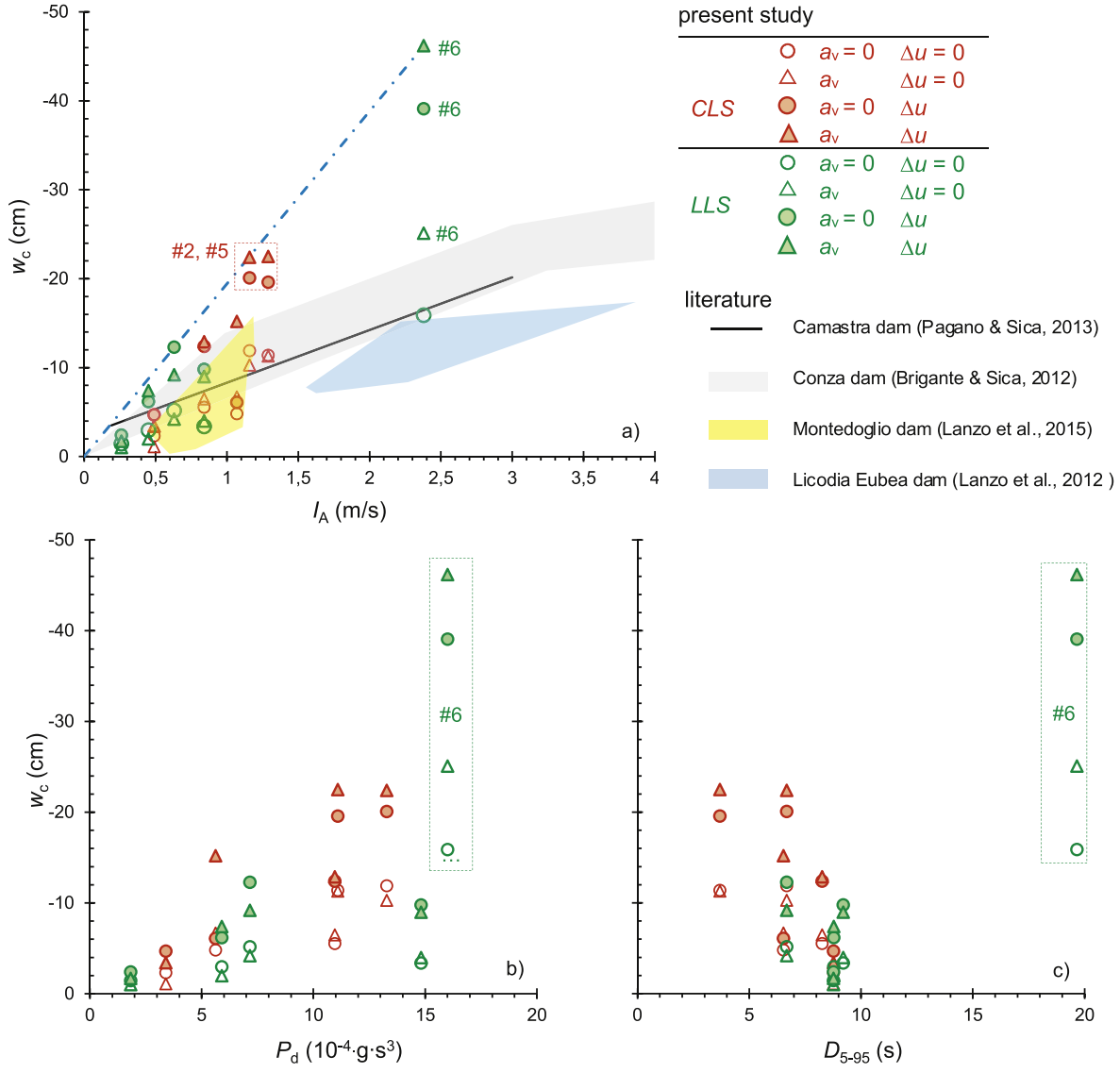

Fig. 18. Plots of earthquake-induced crest settlements computed for the San Pietro dam versus Arias intensity I_A (a), destructiveness potential factor P_d (b) and strong motion duration $D_{5\text{-}95}$ (c).

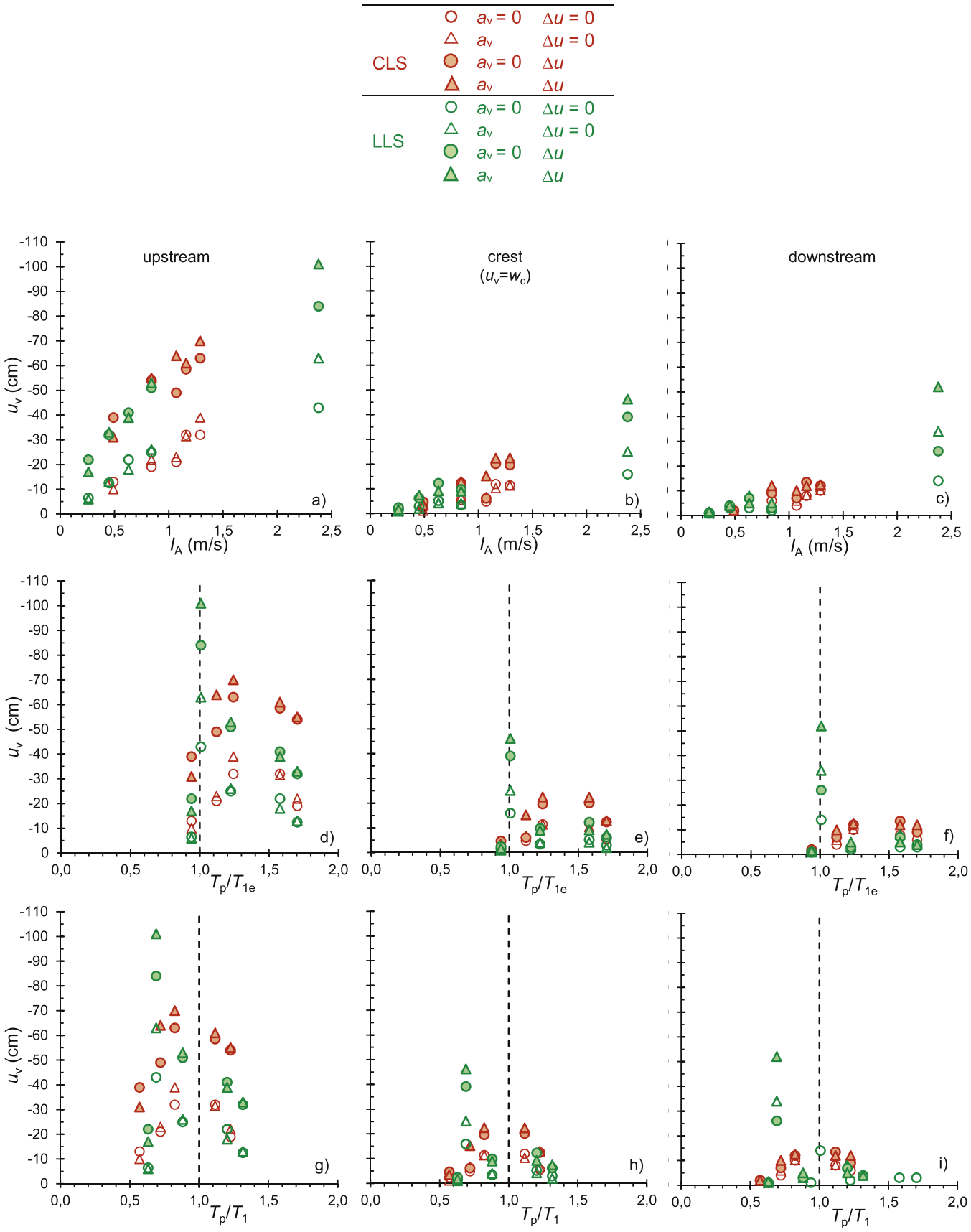

Fig. 19. Influence of the energy and frequency content of the input motion on the vertical displacements of the upstream (a, d, g) and downstream (c, f, i) shells and of the crest (b, e, h) of the San Pietro dam.

values of the computed crest settlement w_c, apparent in Fig. 18, can be ascribed to the more relevant influence of the seismic parameter better describing the energy and frequency content of the input motion.

6.4. Non-linear frequency coupling and performance evaluation

The crest settlement and the vertical displacements computed in the shells, listed in Tables 3 and 4, are plotted in Fig. 19 versus the Arias intensity of the input motion (Fig. 19 a-c), the linear (T_p/T_{1e} – Fig. 19 d-f) and non-linear (T_p/T_1 – Fig. 19 g-i) period ratios. These are computed as the ratio between the predominant period T_p of the input motion (Fig. 6 b) and the natural period of horizontal elastic vibration of the dam T_{1e} or the non-linear period of vibration of the dam T_1, evaluated according to Papadimitriou et al. [18].

Fig. 19 a,c clearly shows that for both upstream and downstream shells, the highest vertical displacements are attained using record #6 as input motion, that is characterised by the highest energy content, confirming that also for the vertical displacements of the shells the Arias intensity describes suitably the effects of seismic shaking in the dam body.

With a few exceptions, the data plotted in Fig. 19 d-i shows a bell-shaped distribution. Also, with the exception of results computed for *LLS* using record #6, Fig. 19 d-f show that the higher vertical displacements (peak of the bell-shaped distribution) generally occur for values of the linear period ratio $T_p/T_{1e} > 1$. The condition $T_p/T_{1e} = 1$, that indicates a perfect matching between the predominant frequency $f_p = 1/T_p$ of the input motion and the first natural frequency of elastic vibration of the dam $f_{1e} = 1/T_{1e}$, should detect possible occurrence of frequency coupling in the case of a nearly elastic dam response, associated to low earthquake-induced shear strains. However, the response of San Pietro dam to the selected input motions is generally characterised by the occurrence of large shear strains, these leading to a strain-dependent reduction of the shear modulus with an increase of the damping ratio, the possible occurrence of pore water pressure build-up and a shifting of the vibration frequency of the dam with an increase in the period ratio.

Herein, this effect was simply accounted for using the non-linear period of vibration of the dam T_1 introduced by Papadimitriou et al. [18], that permits to consider the main aspects of the actual dam response.

Fig. 19 g-i shows that the peak of the bell-shaped distributions of the computed vertical displacements mostly occurs for values of the non-linear period ratio $T_p/T_1 = 1$, confirming that the response of San Pietro dam is ruled by the combined effects of non-linear soil behaviour and frequency coupling between the dam and the selected input motions. This suggests that the non-linear period of vibration of the dam T_1 should be used for a proper selection of the input motions to be used for seismic analyses of earth dams.

According to Aliberti et al. [28] the occurrence of a *LLS* and a *CLS* of the San Pietro dam was checked verifying the conditions $w_c < f$ and $w_c/H < (w_c/H)_y$, being $f = 1.5$ m the service freeboard of the dam, $(w_c/H)_y = 1.25\%$ and 2.25% the threshold values of the normalised crest settlement assumed as a reference for the achievement of the *LLS* and the *CLS*, respectively, and $H = H_d + H_f$ the height of the dam-foundation system, equal to the sum of the dam height $H_d = 48$ m and the thickness of the deformable foundation soil $H_f = 25$ m.

The largest computed crest settlements are equal to $w_c = 22.5$ cm ($w_c/H = 0.31\%$) and $w_c = 46.2$ cm ($w_c/H = 0.63\%$) for the *CLS* (record #2) and the *LLS* (record #6), respectively, and in both cases it is $w_c/H < (w_c/H)_y$ with $w_c < f$.

7. Concluding remarks

The severe seismic actions prescribed by seismic codes for existing dams promoted the need of assessing the seismic performance of a zoned earth-dam through non-linear dynamic analyses. These were performed to check the occurrence of ultimate limit states, assuming a non-linear hysteretic soil model and allowing for excess pore water pressure development. The analyses investigated the role of the vertical component of ground motion, the shear strength and stiffness reduction induced by pore water pressure build-up and the non-linear frequency coupling.

The results have been presented and discussed focusing on the earthquake-induced plastic mechanisms, the acceleration amplification in the dam body, the magnitude of shear strains, the excess pore water pressures and the permanent displacements exhibited by the embankment. The main results can be summarised as follows:

a) amplification of seismic motion is computed in the dam body, with values of horizontal crest acceleration that are, for the case at hand, in a fair agreement with those evaluated using the modified Makdisi & Seed procedure [3];
b) the most severe input motions are those characterised by the larger energy content, that is by the higher values of I_A and P_d, and by frequency contents close to those relevant for the non-linear response of the dam;
c) for the selected input motions, the maximum horizontal and vertical accelerations in the dam are mainly concentrated in the same range of frequencies, with higher values of the horizontal acceleration that thus mainly affect the dam response. Conversely, the vertical component of ground motion has a minor influence in the permanent displacements induced by seismic shaking; possible pore water pressure build up reduces ground motion amplification in the dam body, while increases the permanent dam displacements and the extent of the plastic mechanisms temporarily activated by the seismic shaking;
d) when accounting for pore water pressure build up, large shear strains were computed in the upstream side of the dam, localised along a narrow band extending from the toe of the upstream shell to the crest of the dam, this showing the development of plastic mechanisms temporarily activated by transient mobilisation of the shear strength;
e) the horizontal displacements of the upstream and downstream shells are of opposite sign, indicating bulging of the dam during seismic excitation. The highest displacements are attained in the upstream shell and cannot be reproduced by most of the simplified approaches adopted in the screening-level analyses in that they do not account for the combined effect of cyclic soil behaviour and non-linear frequency coupling governing the dam response;
f) the analyses confirm a nearly linear upper-bound relationship between the crest settlement of the dam and the Arias intensity, which represents a ground motion intensity measure efficient in quantifying the record-to-record variability of seismic-induced displacements [40], suitably describes the overall effects of earthquake loading and, as also shown by recent studies, can be considered as the seismic parameter that provides the most adequate representation of the potential damage induced by a seismic event in an earth dam; accordingly I_A can be used for a selecting appropriate input motions for seismic analyses of earth dams [41];
g) the use of the non-linear period of dam vibration, as introduced by Papadimitriou et al. [18] highlighted that the response of the dam to the selected input motions is governed by the combined effect of non-linear frequency coupling and cyclic soil behaviour, thus

suggesting the use of this period for a proper selection of the input motions;

h) the normalised crest settlements were compared with threshold values of the crest settlement ratio to check the seismic performance of the dam against the occurrence of ultimate limit states. It was verified that, despite the severe seismic inputs adopted in the analyses, a satisfactory seismic performance of San Pietro dam can be envisaged.

Authors' statement

The data that has been used is not confidential.

Declaration of competing interest

The authors declare that they have no known competing financial interests or personal relationships that could have appeared to influence the work reported in this paper.

Acknowledgements

The Authors are grateful to anonymous reviewers for helping to improve the quality of the manuscript.

This work is part of the research activities carried out in the framework of the research project of major national interest, PRIN n. 2017YPMBWJ, on "*Risk assessment of Earth Dams and River Embankments to Earthquakes and Floods* (REDREEF)" funded by the Italian Ministry of Education University and Research (MIUR).

Appendix

To assess the effect of the calibration of the hysteretic model on the seismic response of the dam, three possible different calibration procedures were considered and preliminary dynamic analyses were performed using the numerical model described in the main text.

The calibration procedures were aimed at estimating the parameters b and c (Eq. 1) that best reproduce, respectively, only the normalised shear modulus ($G/G_0 - \gamma$) curves, both normalised shear modulus and damping ($G/G_0 - \gamma$ and D – γ) curves and only the damping (D – γ) curves.

To this purpose, cyclic shear tests were simulated modelling the soil as an elastic-perfectly plastic material obeying the Mohr-Coulomb failure criterion and using the Masing rules to describe the loading-unloading response. The damping D corresponding to any shear strain γ ($D - \gamma$ curve) was then evaluated from the computed hysteresis cycles.

The $D - \gamma$ curves obtained from these three simulations are plotted with solid and dashed lines in Fig. A1 together with the corresponding $G/G_0 - \gamma$ curves; the corresponding three sets of model parameters b and c are listed in Table A1.

In Fig. A1, for comparison, the experimental $G/G_0 - \gamma$ and D – γ data proposed by Rollins et al. [14] (Fig. A1 a), Vucetic & Dobry [16] (Fig. A1 b) and Seed & Idriss [15] (Fig. A3 c) are also plotted using symbols.

It is apparent that, in the range of medium to large shear strains, the stiffness-calibrated hysteretic models (solid black lines in Fig. A1 a-c) lead to damping curves different from those corresponding to the selected set of experimental data (symbols in Fig. A1 a-c): a relevant overprediction of damping is apparent for the soils of the shells (Fig. A1 a) and the core (Fig. A1 b), while damping is slightly underpredicted for the foundation soils (Fig. A1 c).

The results of the analyses obtained using the horizontal component of the record #5 selected for the *CLS*, are presented and discussed in terms of displacement and acceleration response of the dam and distribution of the earthquake-induced shear strain level in the dam body.

Specifically, for the three different calibration procedures:

- Fig. A2 shows the time-histories of the crest settlements (Fig. A2 a), the amplification functions between the crest and the base of the dam (Fig. A2 b) and the profiles of the acceleration ratio $a_{h,max}/a_{h,base}$ along the axis of the dam (Fig. A2 c) superimposed to the envelope provided by Aliberti et al. [28];
- Figs. A3 and A4 show the contour lines of vertical (Fig. A3 a-c) and horizontal (Fig. A3 d-f) permanent displacements and shear strains (Fig. A4) computed in the dam body at the end of shaking;
- Table. A2 lists the maximum vertical and horizontal displacements computed at the end of seismic shaking in the upstream and downstream portions of the dam body as well as at the crest.

As it can be observed, the amplification functions and the acceleration profiles are not significantly affected by the adopted calibration procedure which, conversely, plays a relevant role on the distribution of displacement and shear strains in the dam body. Maximum permanent displacements (Table. A2) evaluated using the set of model parameters obtained reproducing only the normalised shear modulus ($G/G_0 - \gamma$) curves are always larger than those computed using the other two sets of model parameters. Specifically, the relative difference is in the range of about 10–30% and 30–60% for the horizontal and vertical permanent displacement in the shells and is larger than about 40% for the crest settlements.

On the whole, the analysis results led to two fundamental general outcomes: i) the overall dynamic response of the dam in terms of acceleration amplification is not significantly affected by the procedure adopted for the calibration of the hysteretic model; ii) when the hysteretic model is calibrated by fitting only experimental $G/G_0 - \gamma$ curves, the response of the dam is characterised by larger shear strains and crest settlements (with respect to shear strains and displacements evaluated when adopting the other two possible calibration procedures).

So, in order to make a conservative assessment of the dam response, all the analyses described in the paper were performed using the model parameters calibrated on the $G/G_0 - \gamma$ curves.

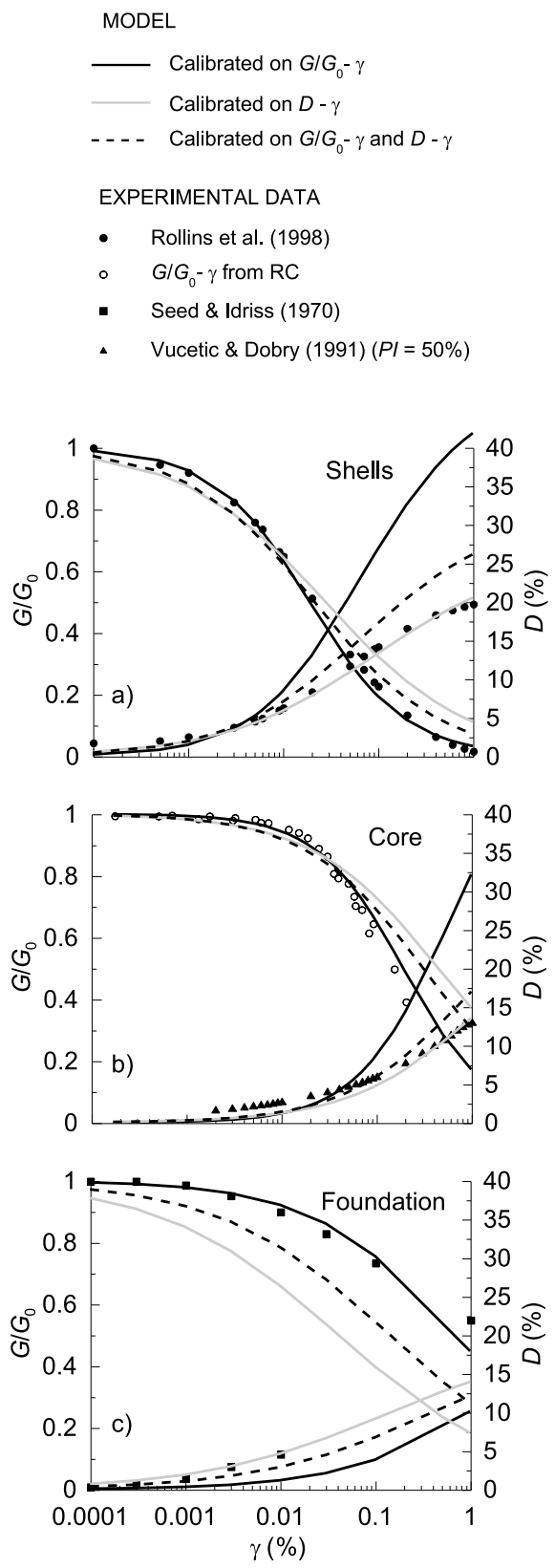

Fig. A1. Calibration of hysteretic model for normalised shear modulus and damping ratio *vs* shear strain for the shells (a), the core (b) and the foundation soil (c) using the normalised stiffness data, the damping $D - \gamma$ data and both $G/G_0 - \gamma$ and $D - \gamma$ data.

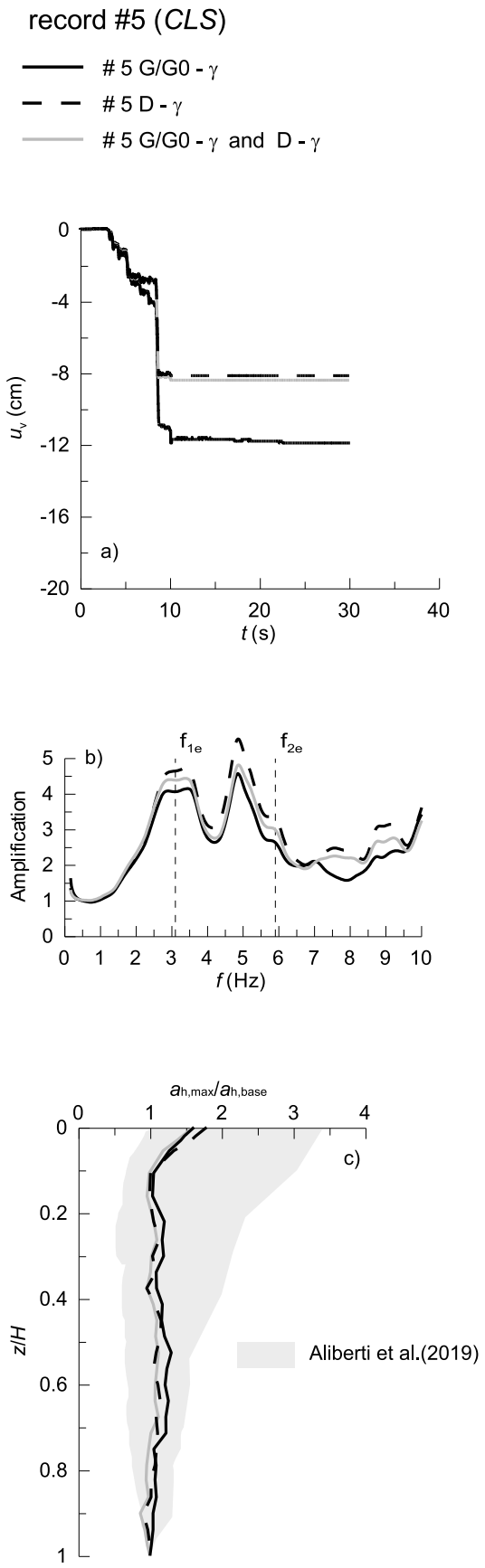

Fig. A2. Influence of hysteretic model calibration on: a) time-histories of crest settlements; b) crest-to-base amplification functions; c) profiles of horizontal normalised accelerations along the dam centre line (record #5 selected for the *CLS*).

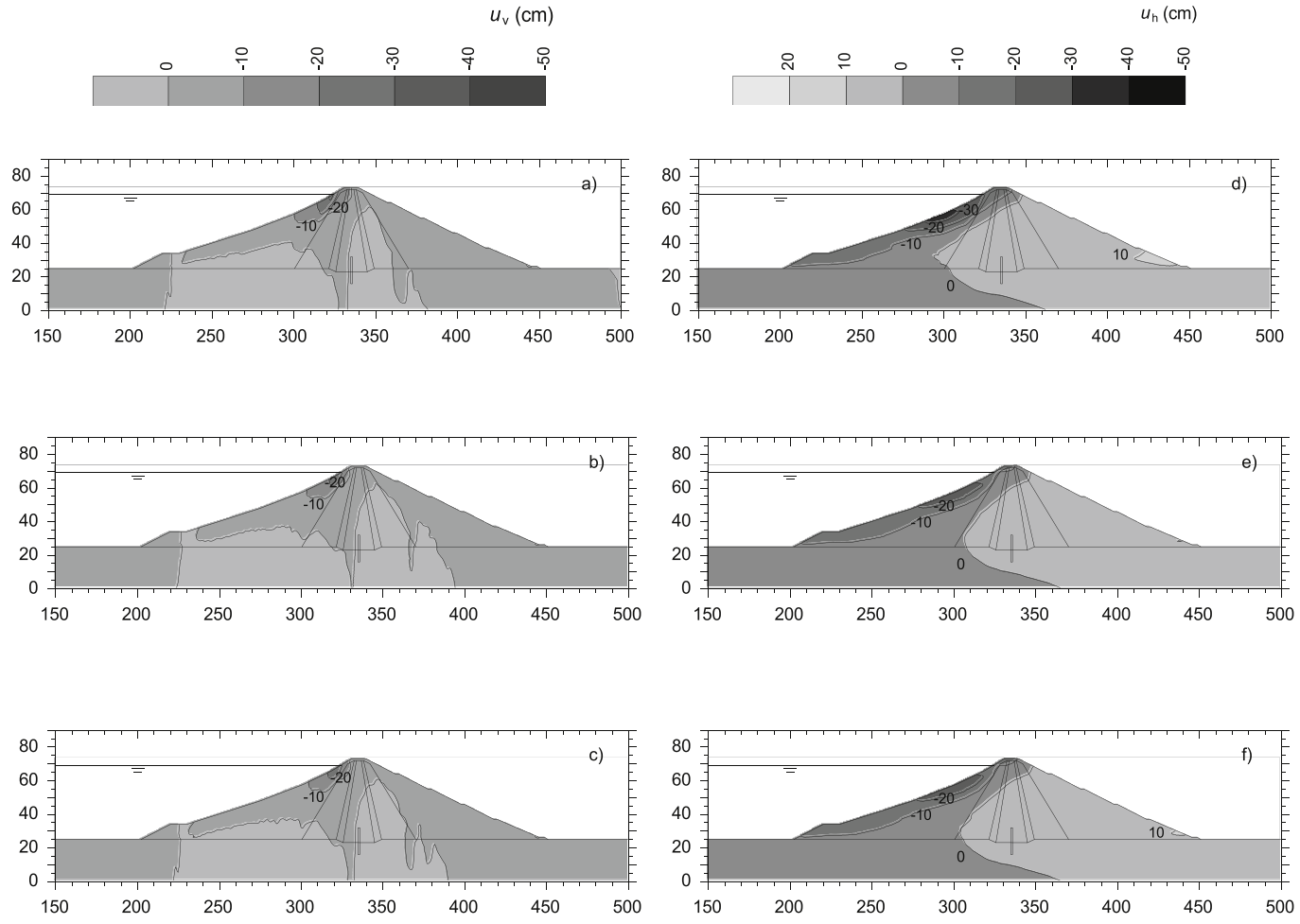

Fig. A3. Influence of the hysteretic model calibration on the distribution of vertical (a-c) and horizontal (d-f) permanent displacements computed for record #5 selected for the *CLS*: calibration against experimental data relative to normalised stiffness ($G/G_0 - \gamma$) (a,d), damping ($D - \gamma$) (b,e) and both normalised stiffness and damping ($G/G_0 - \gamma$ and $D - \gamma$) (c,f).

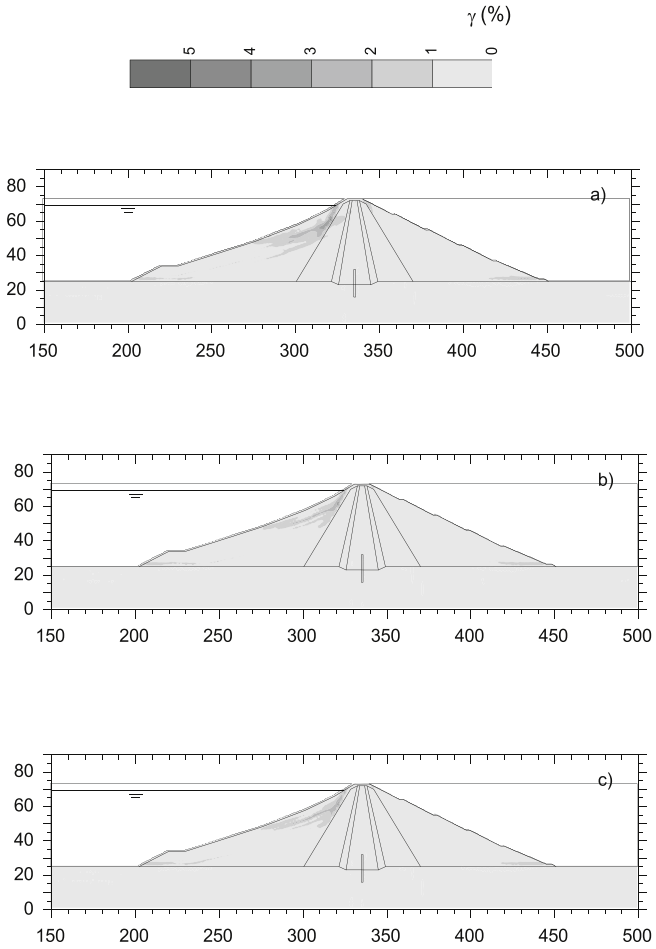

Fig.A4. Influence of the hysteretic model calibration on the distribution of earthquake-induced shear strain computed for record #5 selected for the *CLS*: calibration against experimental data relative to normalised stiffness ($G/G_0 - \gamma$) (a), damping ($D - \gamma$) (b) and both normalised stiffness and damping ($G/G_0 - \gamma$ and $D - \gamma$) (c).

Table A1
Parameters of Eq. (1)

experimental data	material	experimental data	*b*	*c*
$G/G_0 - \gamma$	Shells	Rollins et al. [14] - lower limit	0.506	1.718
	Core	*RC* test results [3]	0.454	0.714
	Foundation	Seed & Idriss [15]	0.748	0.156
$D - \gamma$	Shells	Rollins et al. [14] - lower limit	0.747	1.551
	Core	*RC* test results [3]	0.661	0.345
	Foundation	Seed & Idriss [15]	0.927	1.387
$G/G_0 - \gamma$ and $D - \gamma$	Shells	Rollins et al. [14] - lower limit	0.657	1.668
	Core	*RC* test results [3]	0.614	0.506
	Foundation	Seed & Idriss [15]	0.892	0.845

Table A2
Peak permanent displacements computed (record #5 - *CLS*) at the crest and in the upstream and downstream portions of the dam using different sets of the hysteretic model parameters.

model calibration	upstream		crest	downstream	
	u_v (cm)	u_h (cm)	w_c (cm)	u_v (cm)	u_h (cm)
$G/G_0 - \gamma$	−32	−33	−11.9	−8	12
$D - \gamma$	−25	−25	−8.1	−5	10
$G/G_0 - \gamma$ and $D - \gamma$	−25	−26	−8.4	−6	11

References

[1] NTC18. Aggiornamento delle Norme Tecniche per le Costruzioni. Decreto del Ministero delle Infrastrutture e dei Trasporti, January 17, 2018. G.U. n. 2018;42. February 20, 2018 (in Italian).

[2] NTD14. Norme Tecniche per la progettazione e la costruzione degli sbarramenti di ritenuta (dighe e traverse). June 26, 2014. G.U, vol. 156; 2014. July 8, 2014 (in Italian).

[3] Biondi G, Cascone E, Aliberti D, Rampello S. Screening-level analyses for the evaluation of the seismic performance of a zoned earth dam. Eng Geol 2021;208: 105954.

[4] ICOLD. Design features of dams to effectively resist seismic ground motion. In: Bulletin 120, Committee on seismic aspects of dam design. Paris: International Commission on Large Dams; 2001.

[5] ICOLD. Selecting seismic parameters for large dams. In: Guidelines, revision of bulletin 72, Committee on seismic aspects of dam design. Paris: International Commission on Large Dams; 2010.

[6] Andrianopoulos KI, Papadimitriou AG, Bouckovalas GD, Karamitros DK. Insight into the seismic response of earth dams with an emphasis on seismic coefficient estimation. Comput Geotech 2014;(55):195–210.

[7] Bayraktar A, Kartal ME. Linear and nonlinear response of concrete slab on CFR dam during earthquake. Soil Dynam Earthq Eng 2010;30(10):990–1003.

[8] Yazdani Y, Alembagheri M. Seismic vulnerability of gravity dams in near-fault areas. Soil Dynam Earthq Eng 2017;102:15–24.

[9] Elia G, Amorosi A. Class A prediction of the dynamic behaviour of the San Pietro dam. In: Bauer E, Semprich S, Zenz G, editors. (2009). 2nd international conference on long term behaviour of dams. Graz: Verlag der Technischen Universität Graz; 2009. p. 622–7.

[10] Aliberti D, Biondi G, Cascone E, di Prisco C. Coupled FE seismic analysis of a zoned earth dam. In: Balkema, editor. Earthquake geotechnical engineering for protection and development of environment and constructions. 7th International Conference on Earthquake Geotechnical Engineering. CRC Press Balkema; 2019. p. 1058–65. Rome, Italy.

[11] ITASCA. FLAC – fast Lagrangian analysis of continua. Minneapolis, USA: Itasca Consulting Group; 2011. Version 7.0. User's Guide.

[12] Cundall PA, Hansteen H, Lacasse S, Selnes PB. NESSI, soil structure interaction program for dynamic and static problems. Report: Norwegian Geotechnical Institute; 1980. p. 51508–9.

[13] Stark TD, Beaty MH, Byrne PM, Castro G, Walberg FC, Perlea VG, Axtell PJ, Dillon JC, Empson WB, Mathews DL. Seismic deformation analysis of Tuttle Creek dam. Can Geotech J 2012;49(3):323–43.

[14] Rollins KM, Evans M, Diehl N, Daily W. Shear modulus and damping relationships for gravels. Journal of Geotechnical and Geoenvironmental Engrg 1998;124(5): 396–405.

[15] Seed HB, Idriss IM. Soil moduli and damping factors for dynamic response analysis. Report EERC 70-10, Earthquake Engineering Research Center. Berkeley: University of California; 1970.

[16] Vucetic M, Dobry R. Effect of soil plasticity on cyclic response. Journal of Geotechnical Engineering, ASCE 1991;117(1):89–107.

[17] Dakoulas P, Gazetas G. A class of inhomogeneous shear models for seismic response of dams and embankments. Soil Dynam Earthq Eng 1985;4(4):166–82.

[18] Papadimitriou AG, Bouckovalas GD, Andrianopoulos K. Methodology for estimating seismic coefficients for performance-based design of earth dams and tall embankments. Soil Dynam Earthq Eng 2014;56:57–73.

[19] Martin GR, Finn WD, Seed HB. Fundamentals of liquefaction under cyclic loading. Journal of Geotechnical Engineering Division, ASCE 1975;101(GTS):324–438.

[20] Byrne P. A cyclic shear-volume coupling and pore-pressure model for sand. In: Proc. 2nd Int. Conference on Recent Advances in Geotechnical Earthquake Engineering and Soil Dynamics, Dt. Louis, Missouri. Missouri University of Science and Technology; 1991. p. 47–55. March 1991, Paper No. 1.24.

[21] Tokimatsu K, Seed HB. Evaluation of settlements in sands due to earthquake shaking. Journal of Geotechnical Eng., ASCE 1987;113(8):861–78.

[22] Sun Z, Kong L, Guo A, Alam M. Centrifuge model test and numerical interpretation of seismic responses of a partially submerged deposit slope. Journal of Rock Mechanics and Geotechnical Engineering 2020;12:381–94.

[23] Rathje EM, Ambrahamson NA, Bray JD. Simplified frequency content estimates of earthquake ground motions. Journal of Geotechnical Engineering, ASCE 1998;124 (2):150–9.

[24] Trifunac MD, Brady AG. A study of the duration of strong earthquake ground motion. Bull Seismol Soc Am 1975;65:581–626.

[25] Biondi G, Cascone E, Di Filippo G. Reliability of empirical relationships for the evaluation of the number of equivalent loading cycles. Riv Ital Geotec 2012;46(2): 9–39.

[26] Arias A. A measure of earthquake intensity. In: Hansen, editor. 'Seismic design for nuclear power plants' R. Cambridge, MA: MIT Press; 1970. p. 438–83.

[[27]] Araya R, Saragoni R. Earthquake accelerogram destructiveness potential factor, vol. 2. San Francisco: 8th WCEE; 1984. p. 835–41. 1984.

[28] Aliberti D, Biondi G, Cascone E, Rampello S. Performance indexes for seismic analyses of earth dams. In: Earthquake Geotechnical engineering for protection and development of environment and constructions. 7th International Conference on Earthquake Geotechnical Engineering. CRC Press Balkema; 2019. p. 1066–73. Rome, Italy.

[29] Makdisi F, Seed HB. Simplified procedure for estimating dam and embankment earthquake induced deformations. Journal of Geotechnical Engineering 1978;104 (7):849–67.

[30] Lanzo G, Pagliaroli A, Scasserra G. Effects of ground motion characteristics on seismic response of earth dams: some remarks on duration and vertical shaking. In: SECED Conf. on earthquake risk and engineering, towards a resilient world. SECED; 2015. Cambridge, UK.

[31] Han B, Zdravkovic L, Kontoe S, Taborda DMG. Numerical investigation of the response of the Yele rockfill dam during the 2008 Wenchuan earthquake. Soil Dynam Earthq Eng 2016;88:124–42.

[32] Rampello S, Callisto L, Fargnoli P. Evaluation of slope performance under earthquake loading conditions. Riv Ital Geotec 2010;44(4):29–41.

[33] Biondi G, Cascone E, Rampello S. Evaluation of seismic stability of natural slopes. Riv Ital Geotec 2011;45(1):11–34.

[34] Vecchietti A, Cecconi M, Russo G, Pane V. Seismic vulnerability of a rockfill dam through different displacement-based approaches. J Earthq Eng 2019:1–27.

[3][5]] Meehan CL, Vahedifard F. Evaluation of simplified methods for predicting earthquake-induced slope displacements in earth dams and embankments. Eng Geol 2013;152:180–93.

[36] Pagano L, Sica S. Earthquake early warning for earth dams: concepts and objectives. Nat Hazards 2013;66(2):303–18.

[37] Brigante A, Sica S. Seismic response of a zoned earth dam (case study). Electron J Geotech Eng 2012;17(S):2495–508.

[38] Lanzo G, Verrucci L, Pagliaroli A, Scasserra G. Seismic safety assessment of a concrete gravity dam in Southeastern Sicily. Roma: XXVI Convegno Nazionale di Geotecnica; 2017. p. 1087–95.

[39] Lanzo G, Pagliaroli A, Scasserra G. Selection of ground motion time histories for the nonlinear analysis of earth dams. XVI ECSMGE Geotechnical Engineering for Infrastructure and Development; 2015. p. 2031–6.

[40] Wang G. Efficiency of scalar and vector intensity measures for seismic slope displacements. Front Struct Civ Eng 2012;6(Issue 1):44–52.

[41] Huang D, Wang G. Energy-compatible and spectrum-compatible (ECSC) ground motion simulation using wavelet packets. Earthq Eng Struct Dynam 2017;46: 1855–73.